JOURNAL OF GEOPHYSICAL RESEARCH, VOL. 100, NO. D1, PAGES 1149–1165, JANUARY 20, 1995

Calculation of surface and top of atmosphere radiative fluxes from physical quantities based on ISCCP data sets 1. Method and sensitivity to input data uncertainties

Y.-C. Zhang

Department of Applied Physics, Columbia University, New York

W. B. Rossow and A. A. Lacis

NASA Goddard Institute for Space Studies, New York

Abstract. Upwelling and downwelling, shortwave and longwave radiative fluxes are calculated at the top of the atmosphere and at the surface using a complete radiative transfer model and observations of the physical properties of the surface, atmosphere, and clouds based on the International Satellite Cloud Climatology Project (ISCCP) data sets. Results are obtained every three hours over the whole globe for every third month from April 1985 to January 1989. Sensitivity studies are conducted to assess the uncertainties in calculated fluxes caused by the estimated uncertainties in the measurement or specification of the input quantities. Except in the polar regions, uncertainties in cloud properties are no longer the predominant source of radiative flux uncertainty, even at the surface; rather they produce uncertainties similar in magnitude to those caused by atmospheric and surface properties. The largest uncertainty in upwelling shortwave (SW) fluxes ($\approx 10-15$ W/m^2, regional daily mean) is caused by uncertainties in land surface albedo, whereas the largest uncertainty in downwelling SW at the surface ($\approx 5-10$ W/m^2, regional daily mean) is related to cloud detection errors. The uncertainty of upwelling longwave (LW) fluxes ($\approx 10-20$ W/m^2, regional daily mean) depends on the accuracy of the surface temperature for the surface LW fluxes and the atmospheric temperature for the top of atmosphere LW fluxes. The dominant source of uncertainty in downwelling LW fluxes at the surface ($\approx 10-15$ W/m^2) is uncertainty in atmospheric temperature and, secondarily, atmospheric humidity; clouds play little role except in the polar regions. The uncertainties of the individual flux components and the total net fluxes are largest over land ($15-20$ W/m^2) because of uncertainties in surface albedo (especially its spectral dependence) and surface temperature and emissivity (including its spectral dependence). Clouds are the most important modulator of the SW fluxes, but over land areas, uncertainties in net SW at the surface depend almost as much on uncertainties in surface albedo. Although atmospheric and surface temperature variations cause larger LW flux variations, the most notable feature of the net LW fluxes is the changing relative importance of clouds and water vapor with latitude. Uncertainty in individual flux values is dominated by sampling effects because of large natural variations, but uncertainty in monthly mean fluxes is dominated by bias errors in the input quantities.

1. Introduction

Clouds cause complex changes of the radiative energy exchanges at the top of the atmosphere, within the atmosphere, and at the surface because of large variations of their properties over a wide range of space and time scales. These changes feedback on the forcings for the atmospheric circulations that form clouds. A change in each cloud property affects the shortwave (SW) and longwave (LW) components of the radiation balance differently, so that understanding the link between cloud formation-decay processes and the radiation balance depends on examination of variations of the individual radiative flux components together with changes in each of the key cloud properties. The effects of these cloud-induced radiation variations on the atmospheric circulation are determined by their correlations with perturbations of the three-dimensional temperature field, which may vary with scale. Moreover, cloud variations may be correlated with changes in other properties of the surface and atmosphere, particularly water vapor abundance, that also affect the radiation balance, so these effects must be separated.

The earliest studies of the radiation balance at the top of the atmosphere (TOA), going back to *Brooks* [1949] and *Simpson* [1929], calculated the SW and LW flux components of the balance from estimates of the properties of the atmosphere, clouds, and surface because no direct flux measurements were available. *Budyko* [1974, and references therein] used the same technique to infer the energy budget at the surface. Later, direct satellite measurements of radiation were used to estimate the TOA fluxes [e.g., *Vonder Haar and Suomi,* 1971; *Raschke et al.,* 1973], bypassing the incomplete information about atmosphere, cloud, and surface radiative properties. This approach continues to be refined, producing results most recently from Nimbus 7 [*Kyle et al.,* 1993] and ERBE

Paper number 94JD02747.
0148-0227/95/94JD-02747$05.00

[*Ramanathan et al.*, 1989; *Harrison et al.*, 1990]. Estimates of surface radiative fluxes from satellite radiance measurements are also being made [e.g., *Tarpley*, 1979; *Gautier et al.*, 1980; *Möser and Raschke*, 1983; *Pinker and Ewing*, 1985; *Raschke et al.*, 1987; *Dedieu et al.*, 1987; *Darnell et al.*, 1988; *Gupta*, 1989; *Cess et al.*, 1991; *Li et al.*, 1993; *Breon et al.*, 1994].

Since the focus of earlier studies was on the determination of the total radiation balance, the effects of clouds on that balance were generally only implicit in the results. Recent studies of TOA radiation have been more specific about the role of clouds, using one of two approaches: (1) differencing monthly mean total (full sky) fluxes and the average values obtained under clear conditions [e.g., *Ramanathan et al.*, 1989; *Harrison et al.*, 1990; *Ardanuy et al.*, 1991] or (2) correlating variations of radiative fluxes with observed variations of cloud amount [*Hartmann and Doelling*, 1991; *Sohn and Smith*, 1992]. The latter approach [see also *Cess*, 1976; *Ohring and Clapp*, 1980] assumes that all flux variations are produced solely by cloud amount changes, whereas the former approach assumes that only clouds cause radiative flux variations but does not restrict cloud effects solely to cloud amount variations. Neither of these methods separates variations of the fluxes that are caused by changes of atmospheric and surface properties from those caused by cloud changes.

Flux variations at TOA are not sufficient to diagnose cloud-induced radiative effects on and interactions with the atmospheric and oceanic circulations because the TOA flux balance is not uniquely related to the vertical distribution of radiative heating/cooling in the atmosphere or in the upper ocean [*Webster and Stephens*, 1984]. Moreover, examination of monthly and/or global averaged quantities does not reveal the redistribution of energy by atmosphere-ocean circulations. *Rossow and Lacis* [1990] outlined an approach, based on the earlier technique of calculating fluxes from observed physical quantities, that can address these problems more directly. They concluded that the uncertainties in their calculated fluxes, though smaller than the differences with one climate model, were dominated by the quality of the input data sets and limited by the quality of available validation data sets.

The advent of more accurate global observations of clouds, the atmosphere, the surface and the radiation fluxes at the top of the atmosphere (and some surface radiation flux measurements) makes this older technique attractive again for three reasons. Firstly, this approach naturally separates the effects of clouds on the TOA radiation balance from other factors and allows for direct determination of the variations of radiative fluxes caused by each cloud property. Secondly, this approach also allows for a determination of cloud effects on the complete surface radiation balance, which was done from satellite data for the first time by *Rossow and Lacis* [1990]. Thirdly, calculation of TOA and surface fluxes, together, allows for separation of the total planetary radiation balance into its atmospheric and surface components. Furthermore, this approach may be used to examine the vertical distribution of solar energy deposition and radiative cooling within the atmosphere if enough information about the vertical structure of clouds can be obtained.

To investigate the complete range of cloud radiative effects that are possible requires three characteristics of the data sets: (1) they should cover the whole range of scales encompassing the significant cloud variability, at least mesoscale (200 km, 3 hours) to planetary-climate scale (10,000 km, decade), (2) they should describe the SW and LW cloud radiative effects separately, and (3) they should describe variations of clouds, atmosphere, and surface properties separately. The International Satellite Cloud Climatology Project (ISCCP) cloud data sets, when supplemented by some additional information (section 2), describe the variations of these key physical attributes of clouds, atmosphere, and surface over the required range of time and space scales.

Building on the work of *Rossow and Lacis* [1990], we have developed a more refined calculation of all the individual radiative flux components (see Table 1) that uses these new data sets and a revised radiative transfer model (section 3). Uncertainties in the

Table 1. Definitions of Symbols Representing the Shortwave (SW) and Longwave (LW) Radiative Fluxes, Net Radiative Fluxes for Full-Sky, Overcast-Sky (CLD) and Clear-Sky (CLR) conditions

Symbols	Definition
$S\downarrow_t$, $S\downarrow_s$	downward shortwave fluxes at top of atmosphere and surface, where $S\downarrow_t = \mu_0 S_0$
$S\uparrow_t$, $S\uparrow_s$	upward shortwave fluxes at top of atmosphere and surface
ALB_t, ALB_s	top of atmosphere (planetary) and surface albedos, $ALB_t = S\uparrow_t/S\downarrow_t$ and $ALB_s = S\uparrow_s/S\downarrow_s$
Atmosphere transmissivity	$= S\downarrow_s/S\downarrow_t$
$L\downarrow_t$, $L\downarrow_s$	downward longwave fluxes at top of atmosphere and surface, where $L\downarrow_t = 0$
$L\uparrow_t$, $L\uparrow_s$	upward longwave fluxes at top of atmosphere and surface
Effective temperature	$= (L/\sigma)^{1/4}$, planetary $\equiv L\uparrow_t$, atmospheric $\equiv L\downarrow_s$, surface $\equiv L\uparrow_s$
NS_t	net shortwave flux into top of atmosphere $= S\downarrow_t - S\uparrow_t$
NS_s	net shortwave flux into surface $= S\downarrow_s - S\uparrow_s$
NS_a	net shortwave flux into atmosphere $= NS_t - NS_s$
NL_t	net longwave flux into top of atmosphere $= -L\uparrow_t$
NL_s	net longwave flux into surface $= L\downarrow_s - L\uparrow_s$
NL_a	net longwave flux into atmosphere $= NL_t - NL_s$
N_t	total net flux into top of atmosphere $= NS_t + NL_t$
N_s	total net flux into surface $= NS_s + NL_s$
N_a	total net flux into atmosphere $= N_t - N_s$
CLR-F	flux with no cloud cover; e.g., CLR-$S\uparrow_t$ is the upward shortwave flux at the top of atmosphere with 0% cloud
CLD-F	flux with 100% cloud cover; e.g., CLD-$S\uparrow_t$ is the upward shortwave flux at the top of atmosphere with 100% cloud
CFC-F	cloud flux change is defined as the difference between full-sky and clear-sky flux; e.g., CFC-$S\uparrow_t$ is defined as $S\uparrow_t$ – CLR-$S\uparrow_t$

calculated fluxes attributed to the model treatment of radiation processes are assessed in part by comparison of our radiative model to more detailed calculations. The main purpose of this paper is to assess the uncertainties in the calculated fluxes caused by uncertainties in the input data sets using a set of sensitivity studies (section 4). These results do not represent all sources of uncertainty, however. The overall fidelity of the results is assessed by comparing the calculated fluxes with direct measurements in a companion paper [*Rossow and Zhang*, this issue].

2. Data Sets

The primary input data sets to the radiative transfer model are the ISCCP C1 and C2 data sets [*Rossow and Schiffer*, 1991; *Rossow et al.*, 1991] for every third month from April 1985 to January 1989 (also February and March 1990). ISCCP global data are produced by merging the analyses of narrowband (visible ≈ 0.6 μm and infrared ≈ 11 μm) radiances measured by the network of weather satellites with the TIROS operational vertical sounder (TOVS) daily analysis product produced by National Oceanic and Atmospheric Administration (NOAA) [*Smith et al.*, 1979] and some ancillary data. The main ancillary data set is the weekly snow/ice cover data from NOAA/National Environmental Satellite Data and Information Service (NESDIS) and NAVY/NOAA Joint Ice Center [*Rossow et al.*, 1991]. C1 data are global, three hourly data with a spatial resolution equivalent to 2.5° × 2.5° at the equator. The specific C1 parameters used for the flux calculation are (1) column ozone abundance (O_3), atmospheric temperature profile (T_a) and humidity profile reported as layer precipitable water amount (PW), specified from the surface to the lower stratosphere from TOVS data; (2) surface temperature (T_s) and visible reflectance (R_s) from the ISCCP clear sky radiance composites; and (3) single layer cloud parameters specified by grid cell area averages of fractional cover (Cf), optical thickness (τ), and cloud top temperature (T_c) from the VIS/IR analysis. (VIS/IR analysis refers to the more complete cloud retrieval possible with visible and infrared radiance measurements. Such results are not available at night or over the winter polar regions. Nighttime and winter polar results (IR only) are modified by the observed daytime differences between the VIS/IR and IR-only retrievals.) C2 data are monthly averages of the same C1 parameters which are used to fill in occasionally when C1 parameters are not available.

Additional data sets used to specify parameters not supplied by the ISCCP data sets are (1) a climatology of cloud layer thicknesses as a function of cloud top height, latitude and season based on rawinsonde and surface observations [*Poore et al.*, 1995], (2) climatological aerosol optical thicknesses and compositions adapted from *Charlson et al.* [1991] for the anthropogenic component and from *Toon and Pollack* [1976] for the natural background components, (3) latitude and month-dependent ozone profiles from *London et al.* [1976], (4) global vegetation distribution data and spectral ratios between visible and near-IR albedos for eight vegetation-land surface types and snow/ice as used in the Goddard Institute for Space Studies (GISS) climate general circulation model (GCM) (based on *Matthews*, [1983, 1984]), and (5) a climatology of upper stratospheric temperatures and upper tropospheric humidity from *McClatchey et al.*, [1972].

3. Radiative Model Description

3.1. Description

The radiative transfer model used in these calculations is from the GISS GCM [*Hansen et al.*, 1983] with some modifications to facilitate use of the available data inputs and to make some small improvements. The model treats nongrey gaseous absorptions and thermal emission in a vertically inhomogeneous, multiple-scattering atmosphere and calculates the spectral variation of the upwelling and downwelling SW (nominal wavelength range 0.2 – 5.0 μm) and LW (nominal wavelength range 5.0 – 200.0 μm) fluxes for each atmospheric layer from the top of the atmosphere (TOA = 100 km) to the surface using the correlated k-distribution method [*Lacis and Oinas*, 1991]. (The SW and LW spectral ranges actually overlap, but are treated computationally as noninteractive; that is, SW radiation is absorbed and scattered over the full spectral range (0.2 – 15.0 μm) but does not include the thermally emitted component. Note that the fraction of total SW radiation beyond 5.0 μm is only about 0.5% of the total. Similarly, LW radiation is emitted over the full spectral range (0.2 – 200 μm) to represent the total energy accurately (integral equals σT^4 for unit emissivity) but does not include any solar contribution.) All radiatively significant atmospheric constituents are included. Realistic spectral variations of cloud and aerosol optical properties are obtained from off-line Mie scattering computations [*Hansen and Travis*, 1974] with the spectral cloud and aerosol absorption cross sections merged and tabulated to coincide with the noncontiguous spectral intervals represented in the k-distribution tables for gaseous absorptions.

The k-distribution method implicitly simulates monochromatic spectral integration by grouping wavelengths with similar absorption strengths and permits accurate treatment of overlapping absorption lines of different gases and of nongrey absorption in multiple-scattering media. The numerical accuracy of the k-distribution LW cooling rates is generally within 1% of line-by-line values throughout the troposphere and most of the stratosphere [*Lacis and Oinas*, 1991]. Gaseous absorbers included are H_2O, CO_2, O_3, O_2, NO_2, N_2O, CH_4, CCl_3F, and CCl_2F_3. The well-mixed amounts of the trace gases (CO_2, N_2O, CH_4, CCl_3F, CCl_2F_3) are set to 1980 values [*Hansen et al.*, 1988] and the others at their 1958 values (all amounts can be changed). Absorption coefficients for these gases are a function of temperature, pressure, and absorber amount (see *Lacis and Oinas* [1991] for details). The vertical distribution of H_2O is specified daily at each location from the NOAA TOVS data set. Since TOVS does not provide water vapor amounts above the 300 mbar level (where amounts are very small), water vapor is specified in the upper troposphere by the U.S. Standard Atmosphere (1976) with no seasonal or latitude dependence. The LW continuum absorption by water vapor incorporates the self and foreign broadening contributions in the form given by *Roberts et al.* [1976]. More recent measurements reviewed by *Grant* [1990] suggest 20% less continuum absorption than in the *Roberts et al.*, formulation. On the other hand, Advanced Very High Resolution Resolution Radiometer (AVHRR) window radiances analyzed by *Barton* [1991] imply continuum absorption 20-40% larger. One possible resolution of this disagreement is a much stronger negative temperature dependence of continuum absorption. A recently developed theoretical model of continuum absorption [*Ma and Tipping*, 1991; *Hartmann et al.*, 1993] is in close agreement with the measurements of *Burch and Alt* [1984] upon which the more recent continuum formulations are based. This provides a theoretical basis for both the magnitude and the temperature dependence of continuum absorption; however, the 20% uncertainty still remains. Pending further laboratory verification, we have retained the *Roberts et al.* formulation.

The LW fluxes are computed without scattering using the Mie-calculated absorption cross sections for clouds and aerosols. A first-order correction for LW scattering can be included parametrically by reducing the cloud top emission by the factor $\varepsilon = 1 - R_{CLW}$, where R_{CLW} is the LW cloud reflectivity calculated off line

and tabulated for the k-distribution spectral intervals. In addition, a reflected component of the downwelling flux at cloud top altitude is added to the upwelling radiation. For consistency with ISCCP retrievals (which assume no LW scattering), we set $R_{CLW} = 0$ to turn off this correction.

In the calculation of SW fluxes, scattering effects are treated by a "single Gauss point", doubling/adding method that handles angular integration using one quadrature point and one "extra" angle to represent the solar zenith angle dependence. The phase function is parameterized in terms of upward and downward scattering coefficients to match the solar zenith angle dependence for conservative scattering calculated with the full angle integration of the doubling/adding method [*Hansen and Travis*, 1974]. In this treatment both the direct and the diffuse radiation components are accurately represented. This approach also permits inclusion of the solar zenith angle dependence of surface albedos (if known).

Aerosols and clouds are represented by wavelength-dependent optical thicknesses; all values of optical thickness mentioned in the text are for the reference wavelength of 0.6 μm unless stated otherwise. We modified this approach slightly by introducing a wavelength-dependent Henyey-Greenstein phase function to improve the representation of the spectral dependence of the solar zenith angle dependence of scattering from overlapping clouds and aerosols. The treatment is tuned for the case of conservative scattering over a black surface.

The amounts and optical properties of the following five types of aerosols are specified climatologically: (1) global stratosphere, (2) continental troposphere, (3) oceanic troposphere, (4) desert troposphere, and (5) haze. Each type is a specific mixture selected from 11 kinds of aerosols (in terms of particle size and composition), including silicates, sulfates, sea salt, desert dust, and carbon soot, with amounts and vertical distributions that can be adjusted. The specific aerosol optical properties used (see section 4.1) are based on *Toon and Pollack* [1976] with the abundances of sulfate aerosol adjusted to approximate the anthropogenic component estimated by *Charlson et al.* [1991]. The average aerosol optical thickness (at 0.6 μm wavelength) is 0.066 over oceans and 0.116 over land, giving a global mean value of 0.082. The stratospheric aerosol contributes an optical thickness of 0.012 at all locations.

Before cloud layers are inserted, there are 11 atmospheric layers defined by fixed pressures of 1000 (or surface), 800, 680, 560, 440, 310, 180, 70, 30, 5, 2, and 0 mbar (the top of the atmosphere at 100 km has a pressure of 0.0 mbar). The temperature of the two layers above the 5 mbar level are specified as a function of month and latitude from climatology [*McClatchey et al.*, 1972], while the temperatures of all other layers are specified daily at each location by the NOAA TOVS data set. The number of tropospheric layers varies with the topographic height (surface pressure, P_s) and tropopause height (pressure, P_t). To make the vertical variation of calculated LW fluxes more accurate, the layer mean temperatures are interpolated to give edge temperatures and the temperature profile within each layer is assumed to produce a linear variation of the Planck function [*Carlson et al.*, 1993]. This interpolation also determines the air temperature at the surface.

Surface "skin" temperatures are specified at each location and time from the ISCCP values (T_s). These values are retrieved from narrowband (≈ 11 μm wavelength) radiances assuming unit emissivity for all surfaces; the same assumption is used in the calculation of LW fluxes (although the model can use spectrally varying emissivities, if available). At most latitudes the atmosphere is nearly opaque at wavelengths outside the window region (8 – 14 μm), so that any decrease in upwelling LW flux because of lower surface emissivity is nearly cancelled by an increase of reflected downwelling LW by the higher surface reflectivity. Hence the geographic variation of directly observed brightness temperatures in the window region represents most of the flux variability from the surface [*Conrath et al.*, 1970] (see section 4.2). The radiative model allows for the near-surface air temperatures from TOVS profile extrapolation to differ from the surface skin temperatures.

In the GISS GCM, each 8° × 10° map grid cell is subdivided into as many as four portions to define surface properties: land, land ice, ocean, and sea ice. Land is further subdivided into eight vegetation types (based on *Matthews* [1984]): desert, tundra, grassland, grassland with shrubs, grassland with some trees, deciduous forest, evergreen forest, and rainforest. In addition, all solid surfaces (including sea ice) can be covered with snow characterized by its depth, age, and the masking depth of the underlying vegetation. Our calculations are performed on the ISCCP equal-area grid (equivalent to 2.5° resolution at the equator), so in our first method of specifying surface albedos, the GCM surface types were reformulated with the same procedure [*Matthews*, 1984] for the ISCCP grid. Land albedos are assumed to be Lambertian (but directional albedos can be used if available) and specified in two spectral parts (up to six parts can be used if available) covering the broadband "visible" (≈ 0.2 – 0.7 μm) and broadband near-IR (≈ 0.7 – 5.0 μm). Usually, the radiative model averages the albedos with area weights for each of the grid cell subdivisions to obtain the average visible and near-IR albedos for the whole cell; however, we use the area-weighted average of the spectral ratios for the eight vegetation types (with seasonal adjustments), land ice, sea ice, and fresh snow (maximum depth when present). (Since the spectral response of the Meteosat "visible" channel covers a broader range of wavelengths than the other radiometers used to measure surface reflectances in ISCCP, a special set of spectral ratios is used for areas observed by Meteosat.) Then, the "visible" albedo is set equal to the ISCCP surface visible (≈ 0.6 μm) reflectance (R_s), which is an area-averaged value, and the near-IR albedo is determined from the "visible" albedo and the prescribed (area averaged) spectral ratios. Since the ISCCP values of R_s vary with solar zenith angle, our land surface albedos also vary. In a revised method of determining the spectral ratios (see section 4.2), they are obtained by minimizing the differences between the calculated clear sky land albedos at TOA with Earth Radiation Budget Experiment (ERBE) values [*Harrison et al.*, 1990] as functions of surface type. The ocean directional albedo is specified as a function of solar zenith angle and wind speed (fixed at 2 m s^{-1} in these calculations) by an empirical model defined by a least squares fit of a theoretical model [*Hansen et al.*, 1983] to observed visible ocean reflectances.

ISCCP C1 data report area-averaged cloud properties from measurements in about 50 individual satellite fields of view (pixels about 4 – 7 km in size) in each map grid cell. Although information about the distribution of the cloud properties is available in the C1 data set, for these calculations we use the area-average values to specify the optical thickness (τ) and cloud top temperature (T_c) for a single layer of cloud covering a fraction (Cf) of the grid cell. For some comparisons we use values of τ and T_c (with Cf = 100%) for individual satellite fields of view to calculate fluxes at a spatial scale of about 30 km. Values of τ are averaged with equal weight given to equal intervals of cloud albedo [*Rossow et al.*, 1991]. The radiative transfer model used in the ISCCP retrieval assumes spherical cloud particles composed of liquid water with an effective radius of 10 μm and a size distribution variance of 0.1 [*Rossow et al.*, 1991]. The radiative flux model uses spectrally dependent optical parameters (extinction coefficient, single-scattering albedo, phase function) based on the same microphysical model. The spectral dependence of the optical parameters is related to the visible

value of τ by off-line Mie scattering calculations using the refractive indices tabulated by *Hale and Querry* [1973] for 0.2 to 0.7 μm, *Palmer and Williams* [1974] for 0.7 – 2.0 μm and *Downing and Williams* [1975] for 2.9 – 1000 μm. A microphysical model representing ice clouds is also available, but it is not used in this analysis for consistency with the ISCCP retrievals.

The cloud top pressure (P_c) of the cloud layer is determined from the cloud top temperature, T_c, by linear interpolation in the atmospheric temperature profile (the same value is available from the C1 data set). The cloud base pressure (P_b) is determined by adding a specified pressure increment to P_c. In earlier calculations this pressure increment was fixed at 100 mbar; but in the final results, the increment is specified from a climatology of cloud layer thicknesses as a function of month, latitude, and cloud top location [*Poore et al.*, 1995]. The cloud layer thicknesses in this climatology range from a minimum of ≈ 10 mbar for some low level clouds to over 600 mbar for some higher latitude, upper level clouds with an average value of ≈ 140 mbar. To maintain accuracy in the flux calculations, cloud layers thicker than 140 mbar are divided into a number of layers whose thicknesses are ≤ 140 mbar and the original value of τ is partitioned proportionally to pressure interval in each layer. (The model allows for any number of cloud layers if information is available.) The value of P_b is constrained by a minimum clear layer thickness at the surface, determined from a cloud base height climatology [*Poore et al.*, 1995]. If satisfying this constraint reduces the cloud layer thickness below its climatological minimum (10 mbar), then $P_b = P_s$. If $P_c > P_s$ minus the minimum cloud layer thickness, then $P_c = P_s - P_{min}$ and the atmospheric temperature profile is altered to preserve the value of T_c. A new layer (or layers), defined by P_c and P_b, is inserted into the original C1 atmospheric profile and the profile adjusted so that no layer is thinner than a minimum thickness (5 mbar if pressure is less than 30 mbar, otherwise 20 mbar). The optical thickness of the cloud is assumed to be uniform over the layer.

The solar constant is S_0 = 1367 W/m² [*Hickey et al.*, 1988]. Insolation at TOA ($S\downarrow_t$, see Table 1 for flux symbol definitions) at a particular location and time is a function of the Sun-Earth distance and the solar zenith angle. Formulae for the Sun's coordinates and the equation of time from the *Astronomical Almanac* [1987] are used to calculate the solar zenith angle at each latitude, longitude, and time of day. Each ISCCP observation is interpreted to represent the optical properties of the atmosphere and surface for a 3-hour interval. To obtain the proper daily average SW fluxes (see section 4.5), values of the cosine of the solar zenith angle (μ_0) are calculated at 20-minute intervals and averaged over the 3-hour interval centered on the nominal times of each C1 data set. For example, for a data set with a nominal time of 0600 UTC, the values of μ_0 are averaged over the period 0430 – 0730 UTC. The SW fluxes are then calculated for this average solar zenith angle.

Typically, the ISCCP C1 data set reports cloud and surface observations for about 85% of the globe (covered by 6596 map grid cells) at one time. Tests show (section 4.6) that the best way to fill in the missing values is to interpolate the physical properties of the atmosphere and surface rather than interpolating the calculated fluxes (see also sections 4.4 and 4.5). In addition, since cloud optical thickness is only determined for daytime observations and the cloud top temperature is more accurately determined during daytime, we need to interpolate daytime information into the nighttime. The filling procedure involves four steps: (1) spatial extrapolation, (2) temporal interpolation, (3) substitution of C2 (monthly mean) values, and (4) temporal interpolation of C2 values. Most missing data are filled by step 2.

3.2. Comparison of Radiative Model in ICRCCM

Fluxes calculated by the GISS GCM radiative model for specified atmospheres (mostly clear) have been compared with calculations by line-by-line models as part of the International Comparison of Radiation Codes in Climate Models (ICRCCM) [*Ellingson and Fouquart*, 1991]. Comparisons are still under way, especially for cloudy atmospheres. *Ellingson et al.* [1991] summarize results from the LW flux calculations for 55 clear and 6 cloudy cases. They rank our model as having differences of ($L\downarrow_s$) and NL (tropopause) ≤ 12 W/m² with the line-by-line (LBL) models; a more detailed comparison with the Geophysical Fluid Dynamics Laboratory (GFDL) LBL model for clear atmospheres shows that our model agrees to within a few W/m² for NL_t, NL (tropopause) and NL_s [*Fels et al.*, 1991]. The change in radiative forcing calculated by our model for a doubling of CO_2 abundance agrees with the LBL model results to within 0.3 W/m² out of 6 – 7 W/m² total [*Cess et al.*, 1993]. *Fouquart et al.* [1991] summarize the results from the SW flux calculations for 57 clear and 7 cloudy cases. The higher-resolution models (including the GISS model), as a group, agree with the LBL model results to within 4% for $S\uparrow_t$, $S\downarrow_s$ and NS (cloud); however, differences are about 11% for high solar zenith angles. In summary of the ICRCCM comparisons to date, the individual and net fluxes calculated with the GISS radiative transfer model agree with the LBL model values to within about 5 W/m².

3.3. Model Output Quantities

With all of the input parameters specified from climatology or obtained from ISCCP data sets (either C1 or CX – individual fields of view), all flux components (Table 1) are calculated with the radiative transfer model. All fluxes, together with heating/cooling rates (flux divergences), are calculated for all the atmospheric layers from TOA (100 km) to the surface for each equal-area map cell over the whole globe, every three hours over each month. All fluxes are positive quantities with the direction of the flux indicated by arrow symbols; net fluxes are defined so that positive (negative) values denote heating (cooling). Because each cloud is treated as a single contiguous layer, we focus our attention on the fluxes at TOA and the surface that are less sensitive to cloud vertical structure. The output data set contains the parameters in Table 1 for full sky (actual cloud cover), completely overcast sky (CLD), and clear sky (CLR), as well as all the input C1/C2 parameters (including interpolated values). This combined data set is referred to as the FC data set. For our first studies we have produced FC data sets for every third month from April 1985 to January 1989. In our validation studies, we also compare fluxes calculated for individual satellite fields of view; the ISCCP results at pixel level are referred to as the CX data set and the corresponding flux data set is called FCX.

4. Sensitivity Studies

Our sensitivity studies test how much uncertainty may be caused in the calculated fluxes by uncertainties in the input parameters but do not consider other sources of uncertainty. Each test calculation covers the whole globe for one day [eight UTCs on July 15, 1985] with input parameter values altered (or methodology changed). Daily mean fluxes are compared at each map grid cell either with the original fluxes or with another calculation with a parameter change of the same magnitude but opposite sign. Table 2 summarizes all of the sensitivity test results by showing the global mean and standard deviations of differences of daily mean SW and LW fluxes at TOA and the surface from individual map grid cells.

Table 2. Global Mean Changes in Regional, Daily Mean Fluxes (W/m²) Produced by Changing Input Variables by the Indicated Amounts

Changed Parameter	$\Delta S\uparrow_t$	$\Delta S\uparrow_s$	$\Delta S\downarrow_s$	$\Delta L\uparrow_t$	$\Delta L\uparrow_s$	$\Delta L\downarrow_s$
			Atmospheric Properties			
PW ± 25%	-0.9 (0.7)	-0.5 (0.6)	-2.5 (1.5)	-4.9 (3.2)	—	14.9 (7.2)
Change to new aerosol	-0.8 (1.1)	0.2 (0.4)	1.5 (2.2)	0.2 (0.3)	—	-0.6 (0.6)
T_a ± 2K	0.8 (0.8)	0.0 (0.1)	-0.3 (0.4)	7.3 (2.5)	—	17.4 (3.2)
T_a (first level) ± 2K	0.1 (0.2)	0.0 (0.0)	-0.1 (0.2)	1.6 (1.0)	—	23.0 (6.4)
			Surface Properties			
T_s ± 2K	—	—	—	1.8 (1.4)	22.2 (3.5)	—
Change to new surface albedo (land only)	-9.1 (11.3)	-12.6 (15.2)	-2.6 (4.3)	—	—	—
			Cloud Properties			
Cf ± 11.4%	10.3 (9.0)	-1.9 (3.6)	-12.1 (11.5)	-4.7 (3.9)	0.0 (0.0)	8.3
τ ± 10%	4.9 (4.2)	-0.7 (0.9)	-5.5 (4.7)	-0.8 (0.9)	—	0.7 (0.6)
Night τ ± 20%	—	—	—	-0.6 (0.8)	—	0.5 (0.6)
Interpolated τ ± 20%	1.7 (3.4)	-0.3 (0.8)	-1.9 (4.0)	-1.0 (1.2)	—	0.9 (0.9)
Cold τ – 50%	-0.6 (2.3)	0.1 (0.3)	0.6 (2.2)	0.7 (2.2)	—	-0.2 (0.6)
Change to new μ_0-dependence	0.7 (1.8)	-0.1 (0.4)	-0.7 (1.9)	—	—	—
T_c ± 3K	-1.2 (1.0)	0.0 (0.1)	0.2 (0.3)	5.5 (3.3)	—	2.8 (2.4)
Cold (< 250K) T_c ± 4K	-0.2 (0.4)	0.0 (0.0)	0.0 (0.1)	2.2 (3.6)	—	0.7 (1.6)
Change from fixed to variable cloud layer thickness	-0.2 (0.4)	0.0 (0.0)	0.0 (0.1)	0.5 (1.2)	—	1.7 (3.3)
Increase cloud layer thickness	-0.1 (1.1)	-0.1 (0.1)	-0.6 (1.0)	1.8 (2.3)	—	2.1 (2.2)
Cloud detection test*	-1.4 (9.0)	5.4 (13.4)	6.1 (7.9)	-2.1 (3.2)	-35.0 (41.9)	-3.7 (9.5)

The standard deviations of the flux changes for individual map grid cells are given in parentheses. All input quantities are specified by ISCCP data sets for July 15, 1985.

*For the cloud detection test, the global mean cloud and surface properties change by the following amounts: mean (standard deviation)= -11.4% (8.4%) for Cf; -0.98K (6.8K) for T_c; 0.66 (4.68) for τ; -6.4K (7.7K) for T_s; and -0.010 (0.070) for R_s, including ocean; and -0.024 (0.105) for R_s for land only.

4.1. Atmospheric Properties

Water vapor is the major variable absorber of sunlight in the atmosphere (O_3 absorbs a little more than 20% of the total sunlight absorbed by the atmosphere) and is the primary source of atmospheric opacity blocking LW emission from the surface and causing LW emission from the atmosphere. Water vapor is concentrated near the surface and at lower latitudes. The estimated uncertainty of the water vapor abundances reported in the TOVS data set is about ± 25% [*Smith et al.*, 1979; *Wittmeyer and Vonder Haar*, 1994]. Because TOVS water vapor abundances are determined only in clear or partially cloudy locations, values may be biased low by about 10% in the tropics and by over 25% in the polar regions [*Gaffen and Elliott*, 1993]; however, since the retrieval scheme assigns water vapor amounts based on a climatological relationship between temperatures and humidities [*Smith et al.*, 1979], actual biases are more difficult to determine. Comparison with rawinsonde climatologies suggest biases are less than 10% [*Rossow et al.*, 1991].

The sensitivity test is to calculate the fluxes while varying the precipitable water amount by ± 25% (the range of uncertainty in the water vapor continuum absorption is equivalent to a much smaller uncertainty in water vapor). Thus the flux differences shown in Table 2 are the differences obtained by subtracting the 25% decrease values from the 25% increase values. The largest changes are a global mean increase of 14.9 W/m² for $L\downarrow_s$ and a decrease of 4.9 W/m² for $L\uparrow_t$. The SW fluxes change only by 1 – 3 W/m². Figure 1 shows the latitudinal variations of the differences in $L\downarrow_s$ and CLR-$S\downarrow_s$ caused by increasing the water vapor abundance by 50%. The change in $L\downarrow_s$ is larger in the northern summer midlatitudes than in

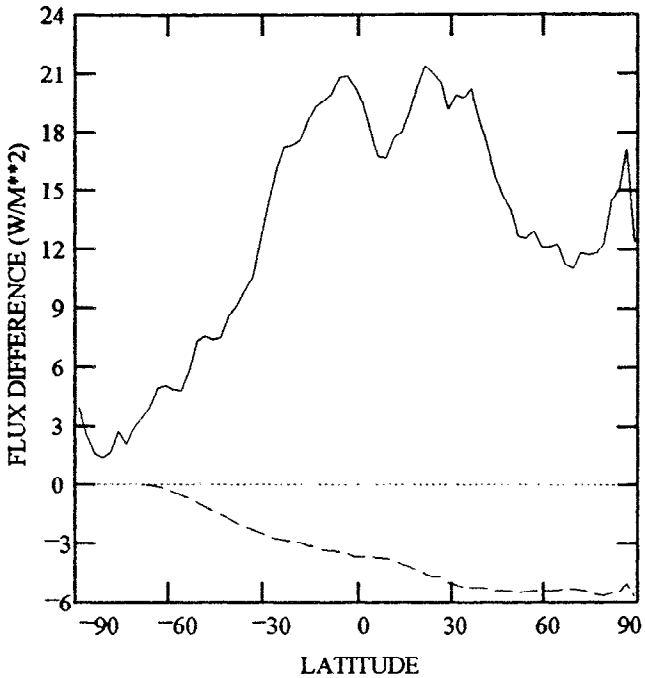

Figure 1. Daily, zonal mean differences in full-sky downwelling surface longwave (LW) flux (solid line) and clear-sky downwelling surface shortwave (SW) flux (dashed line) in watts per meter square caused by a 50% increase in total water vapor abundances. Calculations use input values for July 15, 1985.

the southern winter midlatitudes because the total water vapor abundance and the atmospheric temperature are both higher. The largest change in $L\downarrow_s$ occurs at lower latitudes where the water vapor abundance and atmospheric temperatures are largest; however, the presence of large amounts of cloud reduces the effect in the Inter Tropical Convergence Zone (ITCZ). A similar magnitude uncertainty of the LW fluxes can be caused by an uncertainty of ± 1.3 K in the atmospheric temperatures, especially near the surface (see below). The change in CLR-$S\downarrow_s$ is largest near the north pole in July, even though the water vapor abundance is largest near the equator, because of the longer slant path and higher daily mean value of $S\downarrow_t$ there; however, the change of the annual mean values of $S\downarrow_s$ is largest at low latitudes (about 3 W/m²). Although the magnitude of the effect of water vapor abundance uncertainties on the fluxes is not large, some errors in the TOVS retrievals may vary systematically with climate regime [*Gaffen and Elliott,* 1993; *Wittmeyer and Vonder Haar,* 1994] producing similar systematic errors in the fluxes [see *Rossow and Zhang,* this issue].

The background tropospheric and stratospheric aerosols add very slightly to atmospheric LW opacity but do increase the reflection of SW in clear conditions; their effect is more significant over the darker oceans. While the distribution and properties of acrosols are known qualitatively, the quantitative accuracy is low [*Hansen and Lacis,* 1990]. Our first calculations used a weakly latitude-dependent aerosol optical thickness distribution (Figure 2a) that had a lower mean value over oceans than over land (0.109 versus 0.181). The optical properties were specified as a mix of aerosol types based on *Toon and Pollack* [1976]. In the final version of the model we adopted an aerosol distribution that follows the anthropogenic sulfate aerosol distribution estimated by *Charlson et al.* [1991], combined with a small background of natural aerosol; the main change is a reduction of the acrosol optical thicknesses over ocean to 0.066 (Figure 2a). Figure 2b and Table 2 illustrate the flux differences between these two versions: the decreased aerosol optical thickness in the second version (global mean is reduced from 0.130 to 0.082) increases the global mean $S\downarrow_s$ by about 2 W/m², about 3 W/m² for clear conditions (similar to estimates by *Hansen and Lacis* [1990]). An additional test calculation was made for tropical ocean conditions with the aerosol optical thickness nearly quadrupled to 0.22: $S\downarrow_s$ decreased by about 4 W/m², 6.6 W/m² for clear conditions.

Estimated uncertainties in the TOVS atmospheric temperatures are about ± 2K [*Smith et al.,* 1979; *McMillin,* 1991]. The consequent uncertainty in $L\uparrow_t$ is about 7 W/m² (Table 2) but more than 11 W/m² in the tropics (Figure 3). The uncertainty in $L\downarrow_s$ is about 17 W/m² (Table 2), almost 20 W/m² in the tropics (Figure 3), and is caused primarily by errors in temperature in the lowest atmospheric layer. The next entry in Table 2 shows the effect of changing only the first layer temperature: it is larger because we extrapolate the profile to get the near-surface temperature, so that an increase in one layer changes the lapse rate, too. Figure 4 shows the relative variability of air temperature and humidity obtained from TOVS and from ship measurements [*Young et al.,* 1992] at one place on the equator in February – March 1990. Although the relative magnitude of the TOVS humidity variations (≈ 11%) is only about half of its estimated uncertainty (25%), it is three times larger than measured on the ship (≈ 4%), suggesting that the TOVS humidity variability is dominated by measurement error. The humidity variations do not appear correlated with the temperature variations. The magnitude of the TOVS air temperature variability (≈ 2.5 K) is slightly larger than its estimated uncertainty (≈ 2 K; cf. *McMillin* [1991]) and about twice that measured on the ship. Recalculating $L\downarrow_s$ using the ship-measured temperature or humidity variabilities shows that the 17

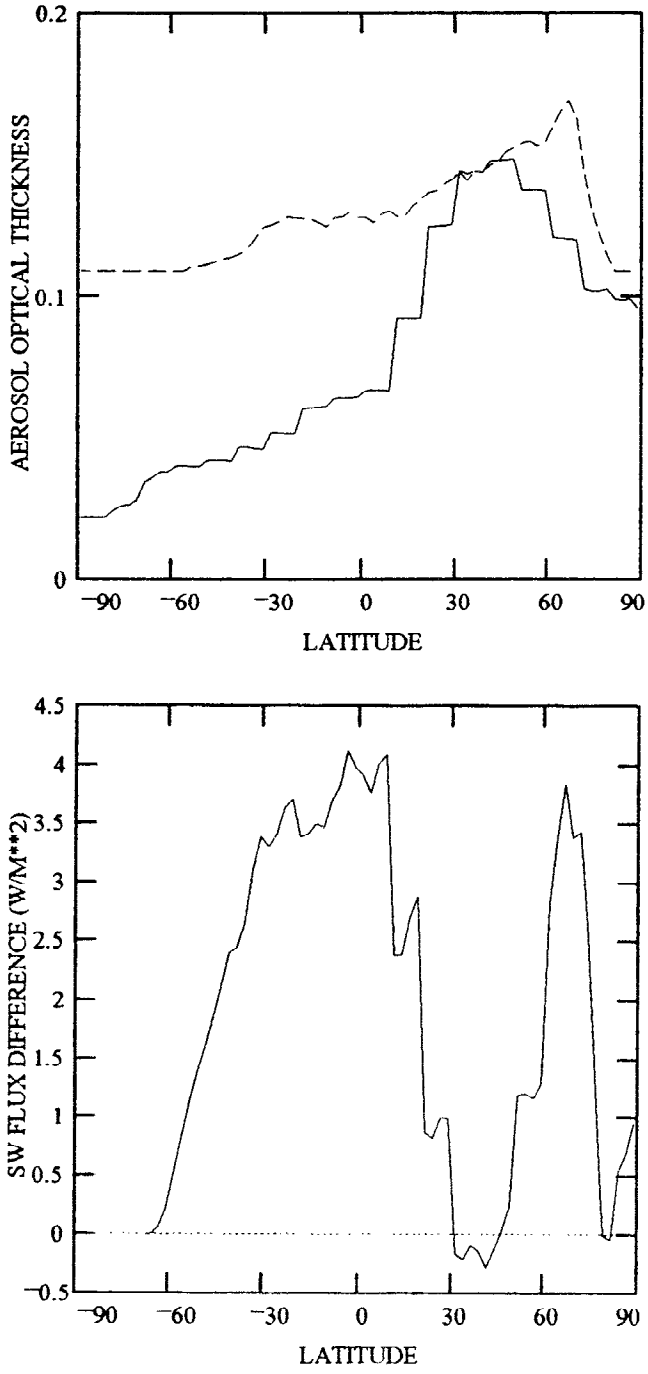

Figure 2. (a) Two models of zonal mean aerosol optical thickness (dashed line = original and solid line = new) and (b) the difference in the daily, zonal mean clear-sky downwelling surface SW flux (W/m²) calculated with these two models (new minus original). Calculations use input values for July 15, 1985.

W/m² difference in variability between our calculated and ship-measured values of $L\downarrow_s$ is caused entirely by the higher air temperature variability in the TOVS data set. The high bias of our values of $L\downarrow_s$ could also be accounted for by lowering the TOVS atmospheric temperature by about 2 K to match the average ship temperatures. A similar comparison study was conducted under colder, drier conditions during the Wisconsin FIRE (First ISCCP Regional Experiment) [*Rossow and Zhang,* this issue]. In this case,

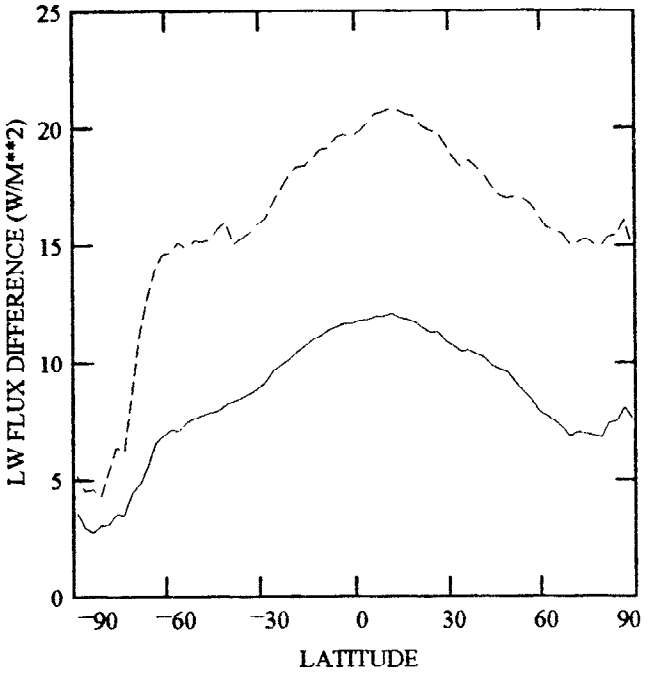

Figure 3. Daily, zonal mean differences in clear-sky upwelling, top of atmosphere (TOA), LW flux (solid line) and full sky downwelling surface LW flux (dashed line) in W/m² caused by a 4 K increase in atmospheric temperatures. Calculations use input values for July 15, 1985.

however, the variability of air temperatures in the TOVS data set underestimates the actual variations such that the calculated values of $L\downarrow_s$ exhibit less day-to-day variation than the surface flux measurements. Thus uncertainties in TOVS atmospheric temperatures are more important to LW flux uncertainties than uncertainties in TOVS water vapor amounts.

4.2. Surface Properties

Errors in the surface temperature, T_s, affect only the upwelling LW fluxes. Comparison of the surface skin temperatures from ISCCP with other measurements of related quantities suggests uncertainties of about 2 K over oceans and about 4 K over land and sea ice; however, some differences are systematic with location and season and can be somewhat larger in particular locations [*Rossow and Garder,* 1993b]. Table 2 shows the LW flux changes for a 4 K increase in T_s: $L\uparrow_s$ increases 22.2 W/m², but $L\uparrow_t$ only increases by 1.8 W/m², indicative of the high LW opacity of the atmosphere.

We note two important considerations. Firstly, other available surface temperature data sets do not report the skin temperature that determines $L\uparrow_s$; instead, sea surface temperature data sets report the temperature of water within 1 – 6 m of the surface [cf. *Schluessel et al.,* 1990; *Wick et al.,* 1992], while land surface temperature data sets report the air temperature at about 2 m height [*Rossow et al.,* 1989; *Rossow and Garder,* 1993b]. Thus, satellite-determined surface temperatures more directly represent the needed physical parameter; but since most current measurements are made at infrared wavelengths, there is a "clear sky" bias in the results [*Rossow et al.,* 1989]. The magnitude of this bias is largest over arid land areas at lower latitudes (highest average solar zenith angles).

Secondly, the spectral dependence of surface emissivity, particularly for arid land [*Buettner and Kern,* 1965; *Prabhakara and Dalu,* 1976; *Salisbury and D'Aria,* 1992, 1994], alters the value of $L\uparrow_s$. Since the atmosphere at most latitudes is nearly opaque at wavelengths outside the range 8 – 14 μm, primarily because of water vapor and CO_2 absorption, the consequent increase in surface reflection of $L\downarrow_s$ nearly cancels the reduction in emission when the emissivity at these wavelengths decreases (in the polar regions where the atmospheric opacity is lower, both lower temperatures and the

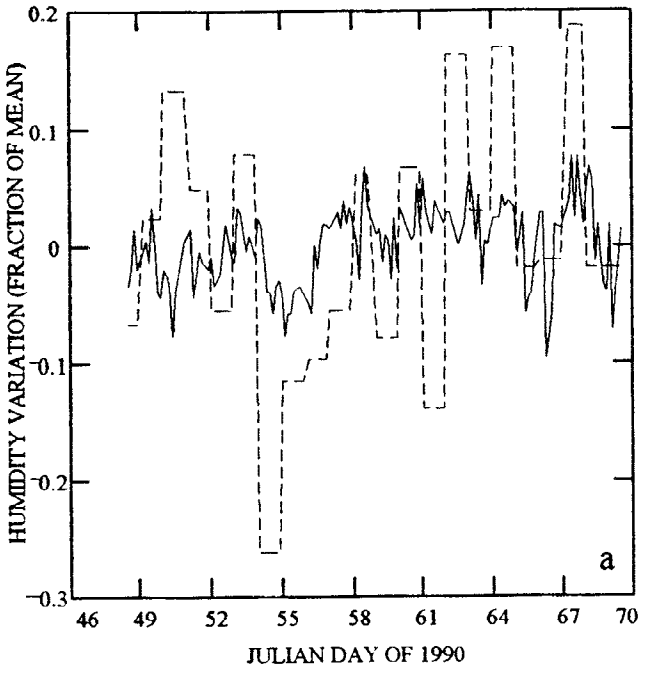

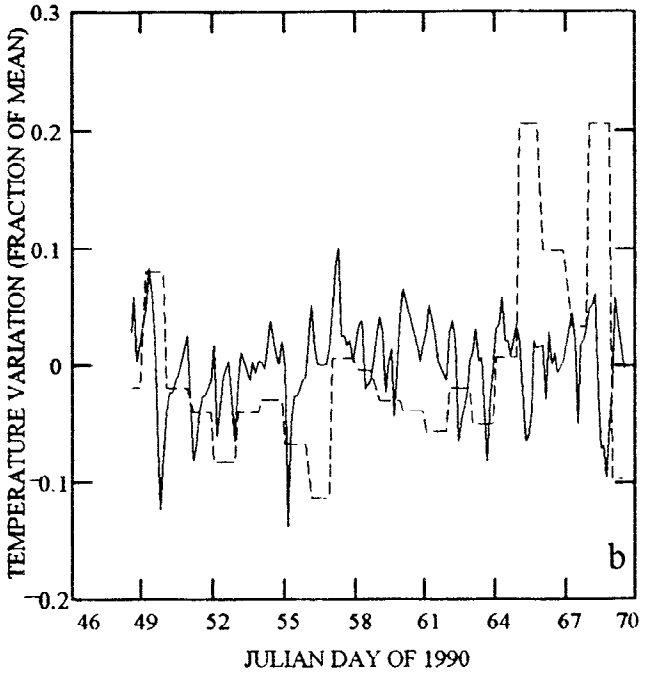

Figure 4. Time record at the ship position of relative variations as fractions of average value of (a) near-surface humidity and (b) surface air temperature. The solid lines show hourly average measurements by shipboard instruments and the dashed lines show daily humidity and temperature values inferred from the TIROS Operational Vertical Sounder (TOVS) analysis. Ship data were obtained by *Young et al.* [1992].

high emissivity of surfaces covered by snow and ice [*Salisbury and D'Aria,* 1994] reduce the magnitude of errors associated with neglecting surface emissivity). Calculations of $L\uparrow_s$ assuming a range of surface emissivities from 1 to 0.8 at wavelengths outside the window shows that $L\uparrow_s$ is reduced by only about 2 – 6 W/m² at surface temperatures ranging from 260 K to 320 K. Thus the most important effect of varying surface emissivity occurs in the 8 to 14 μm wavelength range where satellite instruments directly measure the surface brightness temperature. However, in our analysis an actual surface emissivity <1 reduces the surface temperature retrieved by ISCCP. Using this smaller T_s to calculate $L\uparrow_s$ with emissivity equal to unity at all wavelengths underestimates the LW flux, even though emissivity changes at 8-14 μm produce the largest changes in $L\uparrow_s$, because the emissivity effect integrated over all wavelengths is smaller than estimated by assuming a change of temperature. Literature values of surface emissivities at wavelengths from 5 to 50 μm [*Buettner and Kern,* 1965; *Prabhakara and Dalu,* 1976; *Salisbury and D'Aria,* 1992, 1994] suggest that this bias will be generally $\lesssim$ 10 W/m², except for the most arid surfaces at the highest temperatures. Comparisons of our calculated values of $L\uparrow_t$ with ERBE clear sky values confirm this estimate [*Rossow and Zhang,* this issue].

In our first calculations the values of the spectral ratios used to convert ISCCP values of visible surface reflectance to near-IR albedos were obtained from *Matthews* [1983]; however, in subsequent comparisons of values of $S\uparrow_t$ with ERBE values under clear conditions [*Rossow and Zhang,* this issue], we found that the differences over land were proportional to these ratios and sometimes > 30 W/m². Thus we adjusted the seasonal spectral ratios for eight vegetation types by regression with ERBE clear sky values of $S\uparrow_t$. Table 2 shows that this revision decreases the total values of $S\uparrow_t$ and $S\uparrow_s$ by 9 – 13 W/m² over land and decreases the value of $S\downarrow_s$ by almost 3 W/m². Changes are larger for $S\uparrow_t$ and $S\uparrow_s$ and smaller for $S\downarrow_s$ in clear conditions. The latitude distribution of the change in CLR-$S\uparrow_s$ over land is shown in Figure 5. We estimate that the remaining uncertainty at some locations may still be as large as half the values shown in Figure 5 and Table 2 but generally < 10 W/m². Comparison with ERBE clear sky values of $S\uparrow_t$ suggests that all our surface albedos may still be biased high by about 0.01 overall [*Rossow and Zhang,* this issue].

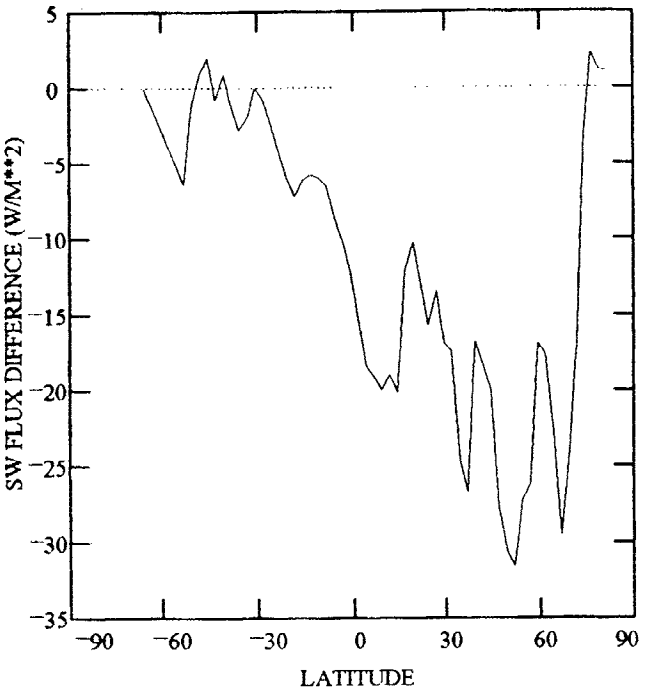

Figure 5. Daily, zonal mean differences in upwelling SW flux (W/m²) at the land surface produced by changing from the initial specification of surface spectral reflectance ratios between visible and near-infrared wavelength ranges to values obtained by comparison with Earth Radiation Budget Experiment (ERBE) clear-sky albedos. Calculations use input values for July 15, 1985.

4.3. Cloud Properties

Table 2 shows the effects on the fluxes produced by increases of each cloud property by twice their estimated uncertainty [*Rossow and Schiffer,* 1991; *Rossow et al.,* 1991]. We use the marginal cloud amounts, ≈ 11%, to represent the uncertainty in Cf (see *Rossow and Garder* [1993a] for definition of this quantity); however, comparison between the ISCCP cloud amounts and those estimated by surface observers suggests that the systematic errors may only be about 5% except for wintertime land areas and the polar regions [*Rossow et al.,* 1993]. An increase of cloud amount by 22.8% (from about 47.6% to 70.4%), holding all other cloud properties constant, causes a 10.3 W/m² increase in $S\uparrow_t$, a 12.1 W/m² decrease in $S\downarrow_s$, and a 2 W/m² decrease in $S\uparrow_s$, such that there is no extra atmospheric heating. Such a low sensitivity to cloud cover variations is caused by the low value of the mean cloud optical thickness (7.27 in this particular test but 5.2 in global annual mean), equivalent to an albedo that is about 2 to 3 times larger than for clear conditions [cf. *Rossow and Schiffer,* 1991]. The increase in cloud amount has less effect on the global mean values of $L\uparrow_t$ (4.7 W/m² decrease) and $L\downarrow_s$ (8.3 W/m² increase). The former effect is reduced and the latter effect is enhanced by water vapor absorption because the majority of clouds are below the effective emission to space level [cf. *Rossow and Schiffer,* 1991].

Uncertainties in the ISCCP values of visible cloud optical thickness (τ) arise from uncertain calibration (about ± 7%), [*Brest and Rossow,* 1992; *Klein and Hartmann,* 1993], neglect of variations of cloud particle size (about ± 12%) [*Han et al.,* 1994], the effects of smaller scale cloud variations (maybe as much as 10%), [*Kobayashi,* 1993], and changes of scattering phase function for ice clouds (as much as 100%) [*Minnis et al.,* 1993]. To complete the flux calculations, we also had to interpolate the daytime measurements of τ into nighttime (and also into locations missing observations). Table 2 shows the changes in the fluxes produced by a 20% increase of all τ values: $S\uparrow_t$ increases by 4.9 W/m² and $S\downarrow_s$ decreases by 5.5 W/m², while the LW fluxes change by < 1 W/m². We also varied the nighttime values of τ by ± 20% to test their effect on daily mean fluxes. The nighttime effect on the LW fluxes is similar to the overall effect because we doubled the magnitude of the change for half of the averaging period. The interpolated values of τ are few enough that even with a 40% change, they cause little variation of global mean values (see section 4.5). To represent possible errors in ice cloud optical thicknesses, we decreased all values of $\tau \leq 4.0$ by 50% for $T_c < 250$ K: Table 2 shows that the global mean "cold τ" effect is < 1 W/m².

The present radiative transfer model uses a Henyey-Greenstein phase function to provide a more flexible means for accurate parameterization of the solar zenith angle dependence with wavelength of SW scattering by cloud and aerosol mixtures than in the original GCM model II [*Hansen et al.,* 1983]. The original GCM parameterization was tuned to model the solar zenith angle dependence of visible radiation for average (τ ~ 5) cloud optical

thicknesses for a Mie scattering phase function for 10 μm spheres. The new scheme accounts better for the changing solar zenith angle dependence with changing cloud and aerosol optical thicknesses. The change increases the global mean value of $S\uparrow_t$ by 0.7 W/m², decreases $S\downarrow_s$ by the same amount (Table 2), and alters their latitude variations (Figure 6). Comparison to full Mie scattering calculations still shows discrepancies in this parameterization that produce a slight overestimate of the cloud spherical albedos with a consequent overestimate of the planetary albedo by as much as 0.005. These remaining discrepancies suggest that the "single Gauss point" approach has reached its practical limit of accuracy to represent the complete dependence of scattering on cloud optical thickness, solar zenith angle, and wavelength.

Uncertainties in cloud top temperatures arise from uncertain calibration (2 – 4 K) [*Brest and Rossow,* 1992; *Klein and Hartmann,* 1993]. Somewhat larger errors occur for optically thin ice clouds because of the error in the retrieved optical thickness (≈ 6 – 10 K), [*Minnis et al.,* 1993]. Larger differences in cloud top temperature also occur when the cloud mass is very low or is diffusely distributed (6 – 10 K), [*Liao et al.,* 1995]; however, the errors in $L\uparrow_t$ are smaller because the value of T_c is determined from the radiance at 11 μm that approximately indicates the effective radiating level in the clouds (the spectral dependence of emission from optically thin clouds can still produce small errors in the fluxes). Table 2 shows the effect on the LW fluxes produced by a 6 K increase in all T_c values: $L\uparrow_t$ increases by 5.5 W/m² and $L\downarrow_s$ increases by 2.8 W/m² because the clouds are moved lower. A lowering cloud level also increases the amount of water vapor above the cloud: the highly reflective cloud causes a fraction of the sunlight to pass twice through the water vapor above it, explaining the changes in SW fluxes, particularly $S\uparrow_t$, which decreases by 1.2 W/m². The ice cloud error is represented by increasing the temperature of all clouds with $T_c <$ 250 K by 8 K; Table 2 shows that the total LW flux changes are still no more than 3 W/m² in this case. Even though the thinner, colder clouds play little role in the total LW fluxes at the top of the atmosphere, their local radiative heating effect may influence atmospheric circulations [*Donner and Kuo,* 1984; *Slingo and Slingo,* 1988; *Randall et al.,* 1989].

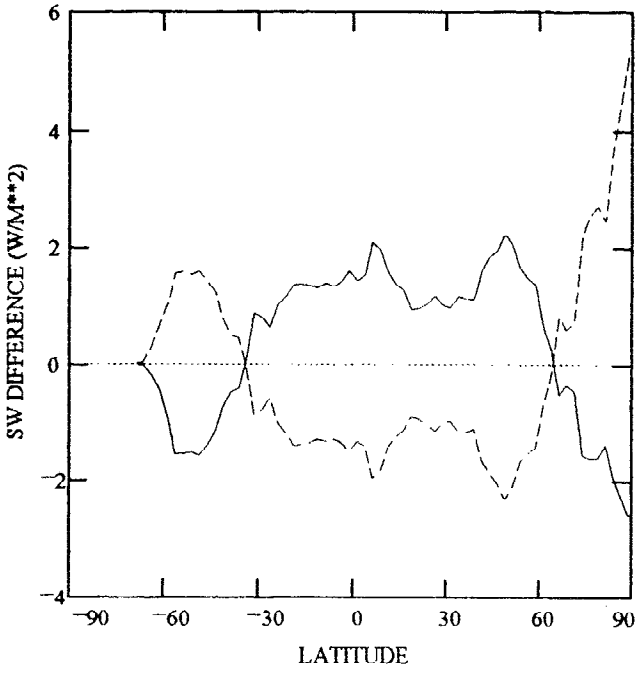

Figure 6. Daily, zonal mean differences in upwelling TOA SW flux (solid line) and downwelling SW flux at the surface (dashed line) in W/m² produced by changing the parameterization of solar zenith angle dependence as a function of cloud optical thickness (new minus original). Calculations use input values for July 15, 1985.

In an earlier version of our calculations we specified cloud base pressures (P_b) as 100 mbar larger than cloud top pressures (P_c). In the current version we use a climatology of cloud layer thicknesses [*Poore et al.,* 1995] to specify cloud base pressures as a function of cloud top pressure, month of year, and latitude over land and water. Cloud layer thicknesses increase monotonically with cloud top height and latitude, ranging from about 2 to 8 km; layer thicknesses of clouds are slightly larger over land than ocean [*Poore et al.,* 1995]. The average cloud layer thickness in the second scheme is about 140 mbar. Table 2 shows that the change of scheme changes only $L\downarrow_s$, increasing it by 1.7 W/m². ($L\uparrow_t$ changes slightly, 0.5 W/m², because insertion of cloud layers with different geometric thicknesses introduces small changes in the atmospheric temperature profile.) Similar sensitivities were obtained using a fixed cloud layer thickness and changing it from 50 to 200 mbar (not shown). Comparison of the average values of P_b predicted using the ISCCP values of P_c and climatological values of cloud layer thickness shows that there is still a low bias in the P_b values used in our calculations (Figure 7). Figure 8 shows the zonal mean change in $L\downarrow_s$ produced by increasing the P_b values by about 200 mbar in the tropics and about 50 – 100 mbar at other latitudes: < 8 W/m² [cf. *Fung et al.,* 1984], about 2 W/m² for the global mean (Table 2). The magnitude of the effects of uncertainties in P_b is smaller in the tropics, except in the highly cloudy ITCZ, than in the polar regions, because water vapor is a more important source of atmospheric opacity.

ISCCP cloud amounts (Cf) show some systematic dependence on μ (cosine of the satellite-viewing zenith angle), which appears to be caused by more frequent detection of optically very thin clouds at lower values of μ [*Rossow and Garder,* 1993b]. Consistent with this interpretation, spatially averaged values of τ and T_c also vary with μ: they both decrease with decreasing μ. We test whether these systematic variations produce systematic variations in the radiative fluxes by examining a region in the Indian Ocean where μ varies from very low values (0.3) at the edge of the Meteosat and GMS satellite views to values near 1.0 where only the NOAA polar orbiters provide data. As can be seen in Figure 9, Cf increases and τ and T_c decrease as μ decreases, but there is no μ dependence apparent in the flux values. In other words the cloud amount and physical cloud property effects on the fluxes offset each other sufficiently to eliminate most of the μ effect.

4.4. International Satellite Cloud Climatology Project (ISCCP) Cloud Detection Errors

In the above tests we have examined the flux uncertainties associated with possible errors in each cloud parameter, separately. The most important source of bias error in the ISCCP results is produced by false or failed cloud detections [*Rossow et al.,* 1993]. Such misclassifications of measured radiances cause correlated errors in the values of T_c, τ, T_s, and R_s as well as in Cf. Hence a better estimate of flux uncertainties associated with uncertainties in the ISCCP cloud amount requires accounting for all the corresponding changes in T_c, τ, T_s, and R_s. This estimate is made possible by the inclusion in the ISCCP C1 data set of parameters related to marginal clouds, clouds that would be missed if the radiance thresholds were doubled: the number of marginally cloudy pixels and the average values of T_c and τ for these pixels. These

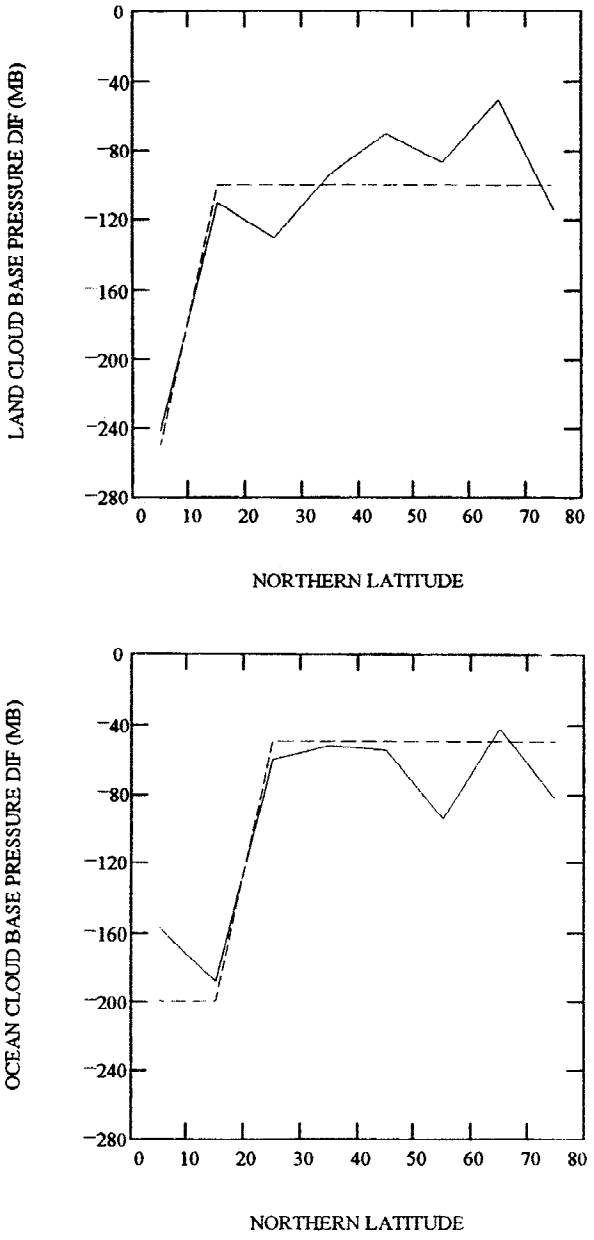

Figure 7. Zonal mean differences in cloud base pressures calculated from ISCCP values of cloud top pressure plus the average cloud layer thicknesses (solid line) over land (left panel) and ocean (right panel) as compared with a cloud base climatology based on rawinsondes [*Poore et al.*, 1995]. Negative values indicate that the predicted cloud base pressures are too low. Dashed lines indicate increases in cloud base pressures used to test flux sensitivity.

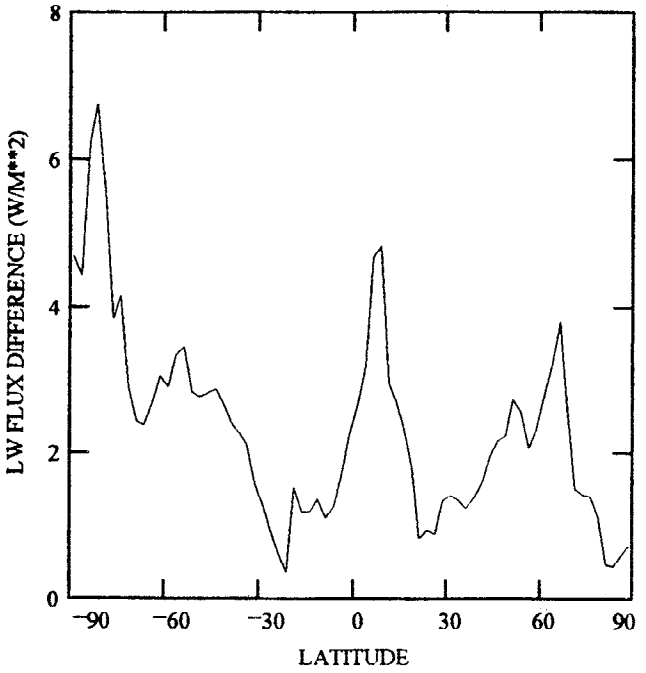

Figure 8. Daily, zonal mean differences in downwelling LW flux at the surface produced by increasing cloud base pressures by an amount indicated by dashed lines in Figure 7. Calculations use input values for July 15, 1985.

values can be used to estimate the first derivative of surface and cloud properties with threshold magnitude [*Rossow et al.*, 1991]. For each location and time, new cloud and surface parameter values are calculated assuming that the marginally cloudy pixels are clear: global mean changes from original to adjusted values are Cf = -11.4%, T_c = -1K, τ = +0.7, T_s = -6.4K, and R_s = +0.01. The last row in Table 2 shows the flux differences produced by these changes in cloud and surface properties. Most changes are only a few watts per meter square except for $L\uparrow_s$, which decreases by 35 W/m² because the value of T_s is lower when cloudy pixels are included in the average. The estimated bias error in ISCCP cloud detections is about half that used in this experiment, except over winter land areas and in the polar regions, where the bias is at least as large as the change used in this test [*Rossow et al.*, 1993]. The relatively large sensitivity of T_s to cloud detection justifies our use of the clear sky composite values for the surface properties which are much less sensitive to analysis errors and have been verified to be accurate within about ± 4 K [*Rossow and Garder*, 1993b]. However, this scheme increases the sensitivity of the other flux components to the other cloud parameters somewhat.

The offsetting effects of errors in cloud detection can also be illustrated by comparing the global, annual mean radiative fluxes, surface, and cloud properties reported in this work with those obtained in the earlier study by *Rossow and Lacis* [1990], shown in Table 3. In the older study the average cloud amount is about 10% lower and the cloud optical thicknesses are about 40% larger (cloud top temperatures are only 1K warmer); the surface albedo is significantly smaller, while the surface temperatures are about the same (slightly warmer land temperatures in the ISCCP results are composed of warmer summertime values partially offset by colder wintertime values). There are consequent systematic differences in the net fluxes, but the changes in radiation balance are only equivalent to net flux differences of about 10 – 15 W/m².

4.5. Daily Integration of SW Fluxes

The ISCCP results are obtained eight times daily, which provides an adequate sample of diurnal (and semidiurnal) variations; however, the number of daytime samples used to calculate daily mean SW fluxes varies with season at higher latitudes from three in winter to five in summer. This can introduce seasonally varying errors in the results. Moreover, the samples are collected with some variation in their temporal separation, so that their distribution is not precisely

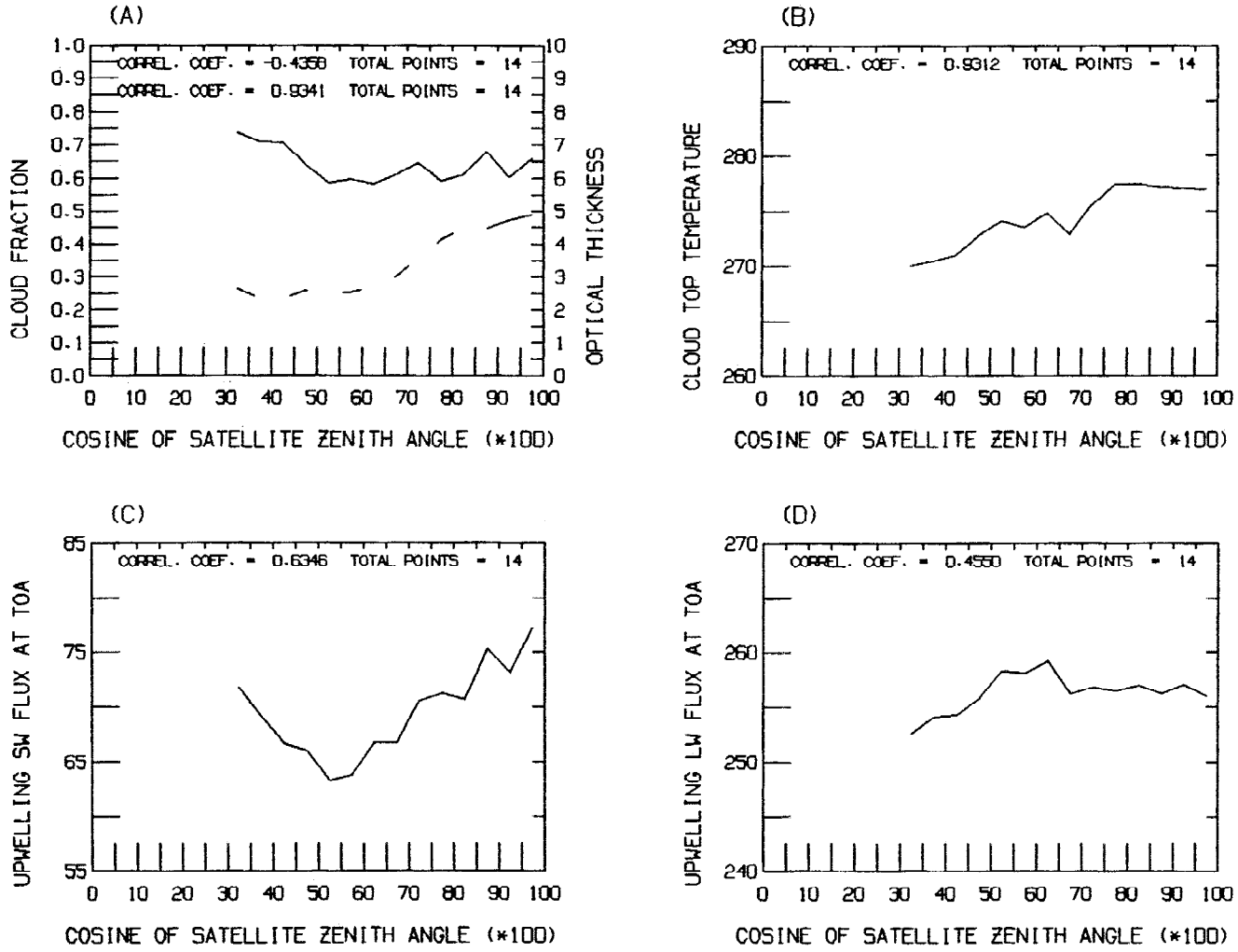

Figure 9. Variations in the Indian Ocean of mean values for July 1986 of (a) cloud amount (solid line) and optical thickness (dashed line), (b) cloud top temperature in K, (c) $S\uparrow_t$ in W/m², and (d) $L\uparrow_t$ in W/m² as functions of μ (cosine of satellite-viewing zenith angle) between low values at the edge of the Meteosat and GMS views and high values from the NOAA polar orbiters.

uniform over the diurnal cycle. We adopted a method to estimate daily mean values from available samples by calculating the SW fluxes at eight particular values of the solar zenith angle that represent the proper time-averaged values over each 3-hour interval. This approach is equivalent to assuming that the atmosphere, cloud, and surface optical properties are constant for three hours, while the solar illumination varies. Other approaches assume that each observation represents conditions at a particular instant, interpolate the SW flux values between observations, or perform weighted averages [cf. *Bishop and Rossow,* 1991]. We tested several other SW integration schemes by creating a synthetic time record of cloud variations from the TOGA-pilot data set [cf. *Rossow and Zhang,* this issue] with 30-minute intervals. This is a very conservative estimate of the errors because SW fluxes are largest at the equator, making the errors largest there, and collapsing day-to-day variability into a period of 1 day should exaggerate the errors associated with unresolved cloud variations. Figure 10 shows the synthesized record of variation of $S\downarrow_s$ that results, along with the variation of cosine of solar zenith angle. The linear average of 48 values is taken as the true daily mean value (= 220.3 W/m²). If the record in Figure 10 is sampled at eight equal intervals, but shifted 1 hour later relative to local noon, and the instantaneous values averaged, the daily mean

Table 3. Comparison of Two Different Analyses of Cloud Properties and Top of Atmosphere and Surface Radiative Fluxes

Quantity	*Rossow and Lacis* [1990]	This Work
Planetary albedo	0.307	0.326
Atmospheric transmissivity	0.540	0.566
Surface albedo	0.086	0.146
Planetary temperature	251.0K	253.2
Atmospheric temperature	280.6K	280.6K
Surface temperature	288.3K	288.8K
Cloud amount	51.1%	60.0%
Cloud top temperature	265.3K	264.4K
Cloud optical thickness	≈ 7*	5.25

All quantities are defined in Table 1 and are global, annual averages.

*The value of this quantity was originally reported as 13.1 by *Rossow and Lacis* [1990], but their value results from a linear average of optical thickness values over space and time. The value shown is estimated using the same averaging as the ISCCP value, which uses nonlinear weights to give equal weight to equal intervals of cloud albedo.

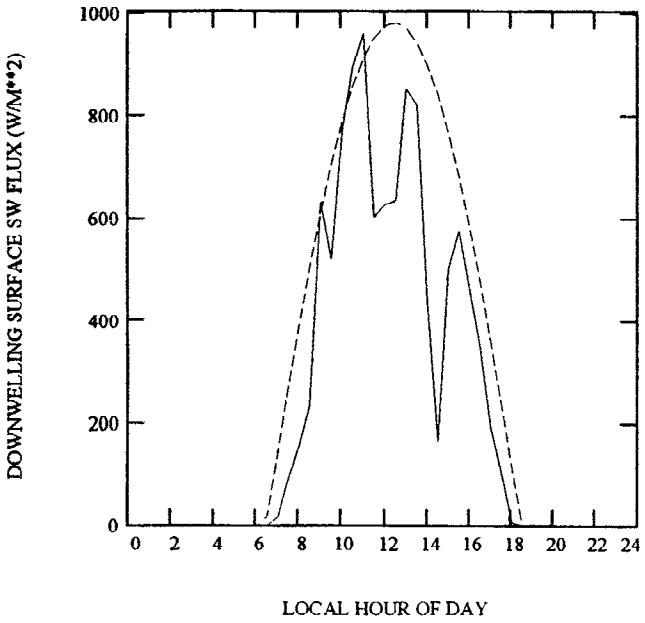

Figure 10. Variations over the day of $S\downarrow_s$ in W/m² (solid line) and μ_0 (cosine of solar zenith angle times 1000, dashed line). The variations of atmospheric and cloud properties at 30-minute intervals used to calculate $S\downarrow_s$ are assembled from observed day-to-day variations in the western Pacific at the equator [see *Rossow and Zhang*, this issue]. The noontime value of μ_0 is $\neq 1$ because the solar declination is not the same as the ship's latitude.

value of $S\downarrow_s$ is about 40 W/m² too high. If the record is sampled eight times but at irregular intervals, the average value of $S\downarrow_s$ is about 60 W/m² too low. Both of these differences are specific to this one case; but typical errors would be roughly similar in magnitude with varying signs. Using the average cosine of solar zenith angles over regular 3-hour intervals produces a daily average value of $S\downarrow_s$ within 7 W/m². Since the errors in all of these sampled results are associated with the values of the solar zenith angle used in the flux calculation, we tried one more case: regular instantaneous sampling symmetric about local noon. This produced the best estimate of the daily mean SW fluxes (differences < 1 W/m²). Thus if not properly represented, the rapid variation of solar zenith angle can be one of the largest sources of uncertainty in daily mean SW fluxes. Uncertainties ~ 10 W/m² are associated with our averaging scheme because we calculated fluxes for eight times UTC instead of in local time. Consequently, there is a longitudinal variation of the errors in our SW fluxes. Assigning the nearest *local* times to produce a regular symmetric sampling would produce even better results.

4.6. Filling Tests

The treatment of missing observations raises the same question: is the best estimate of the average value obtained by averaging over the existing sample, by interpolating flux values between available observations, or by interpolating physical quantities before calculating fluxes. A test was performed by removing a whole day of existing observations and comparing the calculated fluxes obtained from interpolated physical variables to interpolated fluxes and the original fluxes. Globally, errors in the fluxes produced by filling in the physical variables by nearest-value replication are about 2 ± 25 W/m² for SW and 3 ± 15 W/m² for LW; the errors produced by filling in the fluxes by nearest value replication are about 2 ± 40 W/m² for SW and 0 ± 16 W/m² for LW (linear interpolation of the fluxes reduces the rms differences to about 30 W/m² and 10 W/m², respectively). The key conclusion is that the largest variations of atmosphere, cloud, and surface properties occur with location, whereas the largest time variations of fluxes are associated with changes in Cf and τ. The test showed that filling physical properties using a nearby value in time at the same location reduces the rms errors in the calculated SW fluxes but makes little difference for LW fluxes. Tests when comparing to ERBE TOA fluxes also showed that the largest errors in regionally averaged results are produced by missing samples at specific locations; temporal interpolation of physical quantities at such locations improves the result over a simple average. Applying a filling scheme to the data before calculation has the added advantage that all statistics are straightforward; no special averaging schemes are needed because there are no missing values.

The polar regions constitute a more difficult case for the filling procedure in wintertime because the ISCCP analysis does not measure cloud optical thicknesses for more than 2 months in the absence of sunlight. The uncertainties in radiative fluxes under these conditions are examined by comparisons with ERBE measurements at the top of the atmosphere and with surface measurements at Barrow, Alaska, and the south pole [see *Rossow and Zhang*, this issue]. These comparisons showed that the calculated SW fluxes depend more on proper specification of the solar zenith angle and cloud cover variations than on the cloud optical thickness; assuming an average value of $\tau = 2$ produces good agreement with daily mean surface observations at Barrow in October (rms differences ≈ 23 W/m²). This apparent insensitivity to cloud properties is mostly a result of the small magnitude of both the SW and the LW fluxes under polar conditions, but these flux uncertainties, though small in absolute terms, are very large relative to the average flux values. More work is required to improve radiation budgets for the polar regions.

5. Discussion

5.1. Radiative Flux Uncertainties Caused by Input Data Uncertainties

Table 2 summarizes the sensitivities of the calculated flux components to the uncertainties in the input data sets. The largest uncertainty in regional, daily mean SW fluxes (≈ 10 – 15 W/m²) is caused by uncertainties in land surface albedo, since detection uncertainties in cloud cover are generally < 10%, except in the polar regions, and its effects on the fluxes partially offset by correlated uncertainties of cloud optical thicknesses. The accuracy of the upwelling LW flux at the surface is dependent only on the accuracy of the surface temperature and its spectral emissivity; even an error of 2K produces a flux change of about 5 – 10 W/m². Uncertainties in surface emissivity may bias our $L\uparrow_s$ values low by as much as 10 W/m². Land surface temperatures and emissivities are more uncertain than for oceans, causing $L\uparrow_s$ uncertainties that may be as large as 20 – 25 W/m² in some locations. On the other hand the accuracy of the upwelling LW flux at the top of the atmosphere is insensitive to the surface temperature but depends about equally on atmospheric temperature, water vapor abundance, and cloud properties. The effects on $L\uparrow_t$ of cloud detection errors and cloud top temperature partially offset each other. Downwelling LW fluxes at the surface are very sensitive to the input atmospheric data, predominantly the near-surface atmospheric temperature, rather than cloud properties. In general, the uncertainties of the daily mean,

regional values of top of atmospheric flux components (Table 2) and net fluxes (Table 4) are ≤ 10 W/m². The surface net fluxes are more uncertain than the TOA net fluxes; uncertainties in the daily regional mean values of net SW are 10 – 20 W/m² and of net LW, 15 – 25 W/m². The key conclusion of these tests is that the uncertainties in calculated radiative fluxes are no longer dominated by uncertainties in the cloud properties, except in the polar regions [see *Rossow and Zhang*, this issue]. Rather, the remaining uncertainties are contributed in roughly equal parts by the properties of the surface, atmosphere, and clouds.

There are two notable aspects of our findings. Previous studies have stressed the importance of uncertainties in near-surface humidity and cloud base location to uncertainties of $L\downarrow_s$, but we find that atmospheric temperature uncertainties are much more important than either of these. Secondly, the large sensitivity of $L\uparrow_s$ and NL_s to uncertainties of surface temperature indicates the need for careful determinations of the true "skin" temperature, even over oceans, and of temperature and spectral emissivity, particularly over land areas. These results show that use of surface air temperatures over land areas and "bulk" temperatures over oceans can introduce large systematic errors in the surface radiation budget that vary with latitude, season, and time of day.

The results of these sensitivity tests illustrate two distinct advantages of our approach to diagnosis of the radiation balance and cloud effects on it. Firstly, the relative insensitivity of the calculated fluxes to rather large changes in the physical variables (Table 2) indicates that the magnitude of the significant flux variations that drive the atmospheric circulation and constitute the feedbacks on climate perturbations are relatively small, only several tens of W/m². Such small variations imply a requirement for high accuracy (uncertainties less than a few percent) in direct flux measurements if they are going to be used to diagnose the causes of the variations, whereas such a diagnosis is more forgiving for calculated fluxes if the measurement errors for the physical variables can be made as small as about 10% (temperatures need to be accurate to at least 2 K, however).

Secondly, even though the uncertainties of the calculated individual flux components are still significant, uncertainties of the net fluxes are not any larger (Table 4) because the calculated flux components of a net flux all vary with changes in input quantities in physically self-consistent manner. Independent determinations of the individual flux components would produce uncertainties in the net fluxes that are larger than the largest single contribution but smaller than the sum of the individual uncertainties. Since the uncertainties in the calculated net fluxes are dominated by the input data sets, the errors in the individual flux components are correlated through their dependence on the same physical quantities, so that the errors in the net fluxes are similar to the largest individual error (compare Tables 2 and 4).

5.2. Most Significant Influences on Radiative Fluxes

The sensitivity studies also provide a basis for judging which physical variables most influence each of the radiative flux components. Up to now we have considered the flux *uncertainties* associated with measurements of each quantity, but in this section

Table 4. Global Mean Changes in Regional, Daily Mean Net Fluxes (W/m²) Produced by Changing Input Variables in the Same Tests Shown in Table 2

Changed Parameter	ΔNS_t	ΔNS_s	ΔNL_t	ΔNL_s	ΔN_t	ΔN_s
			Atmospheric Properties			
PW ± 25%	0.9 (0.7)	-2.0 (1.2)	4.9 (3.2)	14.9 (7.2)	5.9 (3.3)	12.9 (6.4)
Change to new aerosol	0.8 (1.1)	1.3 (1.8)	-0.2 (0.3)	-0.6 (0.6)	0.6 (0.9)	0.7 (1.5)
T_a ± 2K	-0.8 (0.8)	-0.2 (0.4)	-7.3 (2.5)	17.4 (3.2)	-8.1 (2.5)	17.2 (3.2)
T_a(first level) ± 2K	-0.1 (0.2)	-0.1 (0.2)	-1.6 (1.0)	23.0 (6.4)	-1.7 (1.1)	23.0 (6.4)
			Surface Properties			
T_s ± 2K	—	—	-1.8 (1.4)	22.2 (3.5)	-1.8 (1.4)	-22.2 (3.5)
Change to new surface albedo (land only)	9.1 (11.3)	10.0 (12.4)	—	—	9.1 (11.3)	10.0 (12.4)
			Cloud Properties			
Cf ± 11.4%	-10.3 (9.0)	-10.2 (9.0)	4.7 (3.9)	8.3 (8.0)	(8.3) -5.5	-1.9 (10.1)
τ ± 10%	-4.9 (4.2)	-4.8 (4.1)	0.8 (0.9)	0.7 (0.6)	-4.1 (4.0)	-4.1 (4.1)
Night τ ± 20%	—	—	0.6 (0.8)	0.5 (0.6)	0.6 (0.8)	0.5 (0.6)
Interpolated τ ± 20%	-1.7 (3.4)	-1.6 (3.3)	1.0 (1.2)	0.9 (0.9)	-0.6 (3.4)	-0.7 (3.3)
Cold τ – 50%	0.6 (2.3)	0.6 (2.0)	-0.7 (2.2)	-0.2 (0.6)	-0.2 (1.5)	0.4 (1.8)
Change to new μ_0-dependence	-0.7 (1.8)	-0.6 (1.6)	—	—	-0.7 (1.8)	-0.6 (1.6)
T_c ± 3K	1.2 (1.0)	0.1 (0.3)	-5.5 (3.3)	2.8 (2.4)	-4.4 (3.0)	3.0 (2.4)
Cold (< 250K) T_c ± 4K	0.2 (0.4)	0.0 (0.2)	-2.2 (3.6)	0.7 (1.6)	-2.0 (3.4)	0.7 (1.6)
Change from fixed to variable cloud layer thickness	0.2 (0.4)	0.0 (0.0)	-0.5 (1.2)	1.7 (3.3)	-0.4 (1.0)	1.7 (3.3)
Increase cloud layer thickness	0.1 (1.1)	-0.5 (0.9)	-1.8 (2.3)	2.1 (2.2)	-1.7 (2.2)	1.6 (2.2)
Cloud detection test*	1.4 (9.0)	0.7 (9.9)	2.1 (3.2)	31.3 (45.2)	3.5 (9.8)	31.9 (46.9)

Standard deviations of the flux changes for individual map grid cells are given in parentheses. All input quantities are specified by ISCCP data sets for July 15, 1985.

*For the cloud detection test, the global mean of cloud and surface properties change by the following amounts: mean (standard deviation)= -11.4% (8.4%) for Cf; -0.98K(6.8K) for T_c; 0.66 (4.68) for τ; -6.4K (7.7K) for T_s; and -0.010 (0.070) for R_s, including ocean: and -0.024 (0.105) for R_s for land only.

we consider the direct effect on the fluxes produced by each quantity. There are no surprises, but there are some subtleties. Oceans are so dark relative to clouds (albedo less than half) that clouds are the dominant influence on the SW fluxes over oceans. Because of the strongly anisotropic reflectivity of the ocean surface, clouds even alter $S\uparrow_s$ by changing the relative proportions of direct and diffuse illumination and the spectral distribution of the sunlight reaching the surface [cf. *Webster and Stephens,* 1984]. Over land, average cloud reflectivity is only about 1.5 times larger than for the surface, so that surface albedo is relatively more important to the determination of the SW fluxes. (We have found that on average, uncertainties in land surface albedos are more important than current uncertainties in clouds in causing uncertainty in net surface SW fluxes, however.) Although small, there appears to be a high bias in $S\downarrow_s$ that suggests an underestimate of aerosol optical thicknesses [see *Rossow and Zhang,* this issue]. Water vapor is at least as important to $L\uparrow_t$ as clouds in global averages; but the relative importance of these two factors changes significantly with latitude, with clouds becoming more important at higher latitudes. Over the much cloudier and moister Arctic, clouds play an important role in determining the surface radiation balance [*Curry and Ebert,* 1992], but over the less cloudy and drier Antarctic plateau, water vapor is still important [*Rossow and Zhang,* this issue]. In general, the details of these calculations show that although clouds are generally important to determining the radiation balance, the nature of their influence is strongly dependent on situation and varies with climate regime.

Acknowledgments. Alison Walker provided crucial assistance with data acquisition and development of data processing procedures. Elaine Matthews helped reformulate the land surface spectral albedos based on her vegetation and land use databases. Junhong Wang provided the rawinsonde cloud layer thickness climatology. We had many fruitful conversations with Barbara Carlson, James Bishop, Ehrhard Raschke, Rolf Stuhlmann, Judy Curry, Carol Anne Clayson, and Wayne Darnell. This work was supported by the NASA Global Change Model-Data Assessment program under James C. Dodge in the Earth System Modeling and Global Analysis branch under Robert A. Schiffer and by NSF ATM-9110536 for participation in TOGA-COARE (J.A. Curry, PI).

References

Ardanuy, P. E., L. L. Stowe, A. Gruber, and M. Weiss, Shortwave, longwave and net cloud-radiative forcing as determined from Nimbus 7 observations, *J. Geophys. Res., 96*, 18,537-18,549, 1991.

Astronomical Almanac, *The Astronomical Almanac for 1987*, Nautical Almanac Office, U.S. Government Printing Office, Washington, D. C., 1987.

Barton, I. J., Infrared continuum water vapor absorption coefficients derived from satellite data, *Appl. Opt., 30*, 2929-2934, 1991.

Bishop, J. K. B., and W. B. Rossow, Spatial and temporal variability of global surface solar irradiance, *J. Geophys. Res., 96*, 16,839-16,858, 1991.

Breon, F.-M., R. Frouin, and C. Gautier, Global shortwave energy budget at the Earth's surface from ERBE observations, *J. Clim., 7*, 309-324, 1994.

Brest, C. L., and W. B. Rossow, Radiometric calibration and monitoring of NOAA AVHRR data for ISCCP, *Int. J. Remote Sens., 13*, 235-273, 1992.

Brooks, C. E. P., *Climate Through the Ages*, (revised), 395 pp., Dover, Mineola, N.Y., 1949.

Budyko, M. I., *Climate and Life*, edited by D.H. Miller, 508 pp., Academic, San Diego, Calif., 1974.

Buettner, K. J. K., and C. D. Kern, The determination of infrared emissivities of terrestrial surfaces, *J. Geophys. Res., 70*, 1329-1337, 1965.

Burch, D. E., and R. L. Alt, Continuum absorption by H_2O in the 700-1200 cm^{-1} and 2400-2800 cm^{-1} windows., *Tech. Rep., AFGL-TR-84-0128,* Hanscom AFB, Mass., 1984.

Carlson, B. E., A. A. Lacis, and W. B. Rossow, Tropospheric gas composition and cloud structure of the Jovian North Equatorial Belt, *J. Geophys. Res., 98*, 5251-5290, 1993.

Cess, R. D., Climate change: An appraisal of atmospheric feedback mechanisms employing zonal climatology, *J. Atmos. Sci., 33*, 1831-1843, 1976.

Cess, R. D., E. G. Dutton, J. J. DeLuisi, and F. Jiang, Determining surface solar absorption from broadband satellite mesurements for clear skies: Comparison with surface measurements, *J. Clim., 4*, 236-247, 1991.

Cess, R. D., et al., Intercomparison of CO_2 radiative forcing in atmospheric general circulation models, *Science, 262*, 1252-1255, 1993.

Charlson, R. J., J. Langner, H. Rodhe, C. B. Leovy, and S. G. Warren, Perturbation of the Northern Hemisphere radiative balance by backscattering from anthropogenic sulfate aerosols, *Tellus, 43(AB)*, 152-163, 1991.

Conrath, B. J., R. A. Hanel, V. G. Kunde, and C. Prabhakara, The infrared interferometer experiment on Nimbus 3, *J. Geophys. Res., 75*, 5831-5857, 1970.

Curry, J. A., and E. E. Ebert, Annual cycle of radiation fluxes over the Arctic Ocean: Sensitivity to cloud optical properties, *J. Clim., 5*, 1267-1280, 1992.

Darnell, W. L., W. F. Staylor, S. K. Gupta, and F. M. Denn, Estimation of surface insolation using sun-synchronous satellite data, *J. Clim., 1*, 820-835, 1988.

Dedieu, G., P. Y. Deschamps, and Y. H. Kerr, Satellite estimation of solar irradiance at the surface of the Earth and of surface albedo using a physical model applied to METEOSAT data, *J. Clim. Appl. Meteorol., 26*, 79-87, 1987.

Donner, L. J., and H.-L. Kuo, Radiative forcing of stationary planetary waves, *J. Atmos. Sci., 41*, 2849-2868, 1984.

Downing, H. D., and D. Williams, Optical constants of water in the infrared, *J. Geophys. Res., 80*, 1656-1661, 1975.

Ellingson, R. G., and Y. Fouquart, The intercomparison of radiation codes in climate models: An overview, *J. Geophys. Res., 96*, 8925-8927, 1991.

Ellingson, R. G., J. Ellis, and S. Fels, The intercomparison of radiation codes used in climate models: Longwave results, *J. Geophys. Res., 96*, 8929-8953, 1991.

Fels, S. B., J. T. Kiehl, A. A. Lacis, and M. D. Schwarzkopf, Infrared cooling rate calculations in operational general circulation models: comparisons with benchmark computations, *J. Geophys. Res., 96*, 9105-9120, 1991.

Fouquart, Y., B. Bonnel, and V. Ramaswamy, Intercomparing shortwave radiation codes for climate studies, *J. Geophys. Res., 96*, 8955-8968, 1991.

Fung, I. Y., D. E. Harrison, and A. A. Lacis, On the variability of the net longwave radiation at the ocean surface, *Rev. Geophys., 22*, 177-193, 1984.

Gaffen, D. J., and W. P. Elliott, Column water vapor content in clear and cloudy skies, *J. Clim., 6*, 2278-2287, 1993.

Gautier, C., G. Diak, and S. Masse, A simple physical model to estimate incident solar radiation at the surface from GOES satellite data, *J. Appl. Meteorol., 19*, 1005-1012, 1980.

Grant, W. B., Water vapor absorption coefficients in the 8-13 μm spectral region: A critical review, *Appl. Opt., 29*, 451-462, 1990.

Gupta, S. K., A parameterization for longwave surface radiation from sun-synchronous satellite data, *J. Clim., 2*, 305-320, 1989.

Hale, G. M., and M. R. Querry, Optical constants of water in the 200-nm to 200-μm wavelength region, *Appl. Opt., 12*, 555-563, 1973.

Han, Q.-Y., W. B. Rossow, and A. A. Lacis, Near-global survey of effective cloud droplet radii in liquid water clouds using ISCCP data, *J. Clim., 7*, 465-497, 1994.

Hansen, J. E., and A. A. Lacis, Sun and dust versus greenhouse gases: an assessment of their relative roles in global climate change, *Nature, 346*, 713-719, 1990.

Hansen, J. E., and L. D. Travis, Light scattering in planetary atmospheres, *Space Sci. Rev., 16*, 527-610, 1974.

Hansen, J., G. Russell, D. Rind, P. Stone, A. Lacis, S. Lebedeff, R. Ruedy, and L. Travis, Efficient three-dimensional models for climate studies: Models I and II, *Mon. Weather Rev., 111*, 609-662, 1983.

Hansen, J., I. Fung, A. Lacis, D. Rind, S. Lebedeff, R. Ruedy, G. Russell, and P. Stone, Global climate changes as forecast by the Goddard Institute for Space Studies three-dimensional model, *J. Geophys. Res., 93*, 9341-9364, 1988.

Harrison, E. F., P. Minnis, B. R. Barkstrom, V. Ramanathan, R. D. Cess, and G. G. Gibson, Seasonal variation of cloud radiative forcing derived from the Earth Radiation Budget Experiment, *J. Geophys. Res., 95*, 18,687-18,703, 1990.

Hartmann, D. L., and D. Doelling, On the net radiative effectiveness of clouds, *J. Geophys. Res., 96*, 869-891, 1991.

Hartmann, J. M., M. Y. Perrin, Q. Ma, and R. H. Tipping, The infrared continuum of pure water vapor: Calculations and high-temperature measurements, *J. Quant. Spectrosc. Radiat. Transfer, 49*, 675-691, 1993.

Hickey, J. R., B. M. Alton, H. L. Kyle, and D. V. Hoyt, Total solar irradiance measurements by ERB/Nimbus 7, A review of nine years, *Space Sci. Rev., 48*, 321-342, 1988.

Klein, S. A., and D. L. Hartmann, Spurious trends in the ISCCP C2 data set, *Geophys. Res. Lett., 20*, 455-458, 1993.

Kobayashi, T., Effects due to cloud geometry on biases in the albedo derived from radiance measurements, *J. Clim., 6*, 120-128, 1993.

Kyle, H. L., et al., The Nimbus earth radiation budget (ERB) experiment: 1975 to 1992, *Bull. Am. Meteorol. Soc., 74*, 815-830, 1993.

Lacis, A. A., and V. Oinas, A description of the correlate k-distribution method for modeling non-grey gaseous absorption, thermal emission, and multiple scattering in vertically inhomogenous atmospheres, *J. Geophys. Res., 96*, 9027-9063, 1991.

Li, Z., H. G. Leighton, K. Masuda, and T. Takashima, Estimation of SW flux absorbed at the surface from TOA reflected flux, *J. Clim., 6*, 317-330, 1993.

Liao, X., D. Rind, and W. B. Rossow, Comparison between SAGE II and ISCCP high-level clouds, 2, Cloud vertical structure, *J. Geophys. Res.*, in press, 1995.

London, J. R., B. D. Bojkov, S. Oltmans, and J. F. Kelly, Atlas of the Global Distribution of Total Ozone, July 1957-July 1967, *NCAR Tech. Note 113 + STR*, 276 pp., Nat. Cent. for Atmos. Res., Boulder, Colo., 1976.

Ma, Q., and R. H. Tipping, A far wind line shape theory and its application to the water continuum absorption in the infrared region, 1, *J. Chem. Phys., 95*, 6290-6301, 1991.

Matthews, E., Global vegetation and land use: New high-resolution data bases for climate studies, *J. Clim. Appl. Meteorol., 22*, 474-487, 1983.

Matthews, E., Prescription of land-surface boundary conditions in GISS GCM II: A simple method based on high-resolution vegetation data bases, *NASA Tech. Memo. 86096*, 20 pp., 1984.

McClatchey, R. A., R. W. Fenn, J. E. A. Selby, F. E. Volz, and J. S. Garing, Optical Properties of the Atmosphere, *AFCRL-72-0497, Environ. Res. Pap., 411*, 108 pp., Air Force Cambridge Res. Labs., Hanscom Air Force Base, Mass., 1972.

McMillin, L. M., Evaluation of a classification method for retrieving atmospheric temperatures from satellite measurements, *J. Appl. Meteorol., 30*, 432-446, 1991.

Minnis, P., P. W. Heck, and D. F. Young, Inference of cirrus cloud properties from satellite-observed visible and infrared radiances, 2, Verification of theoretical cirrus radiative properties, *J. Atmos. Sci., 50*, 1305-1322, 1993.

Möser, W., and E. Raschke, Mapping of global radiation and of cloudiness from METEOSAT image data, *Meteorol. Rundsch., 36*, 33-41, 1983.

Ohring, G., and P. F. Clapp, The effect of changes in cloud amount on the net radiation at the top of the atmosphere, *J. Atmos. Sci., 37*, 447-454, 1980.

Palmer, K. F., and D. Williams, Optical properties of water in the near infrared, *J. Opt. Soc. Am., 64*, 1107-1110, 1974.

Pinker, R. T., and J. A. Ewing, Modeling surface solar radiation: Model formulation and validation, *J. Clim. Appl. Meteorol., 24*, 389-401, 1985.

Poore, K., J.-H. Wang, and W. B. Rossow, Climatology of cloud layer thicknesses from a combination of surface and upper air observations, *J. Clim.*, in press, 1995.

Prabhakara, C., and G. Dalu, Remote sensing of the surface emissivity at 9 μm over the globe, *J. Geophys. Res., 79*, 5039-5044, 1976.

Ramanathan, V., R. D. Cess, E. F. Harrison, P. Minnis, B. R. Barkstrom, E. Ahmad, and D. Hartmann, Cloud-radiative forcing and climate: Results from the Earth Radiation Budget Experiment, *Science, 243*, 57-63, 1989.

Randall, D., Harshvardhan, D. A. Dazlich, and T. C. Corsetti, Interactions among radiation, convection and large-scale dynamics in a general circulation model, *J. Atmos. Sci., 46*, 1943-1970, 1984.

Raschke, E., T. H. Vonder Haar, W. R. Bandeen, and M. Pasternak, The annual radiation balance of the earth-atmosphere system during 1967-70 from Nimbus 3 measurements, *J. Atmos. Sci., 30*, 341-364, 1973.

Raschke, E., A. Gratzki, and M. Rieland, Estimates of global radiation at the ground from the reduced data sets of the International Satellite Cloud Climatology Project, *J. Climatol., 7*, 205-213, 1987.

Roberts, R. E., J. E. A. Selby, and L. M. Biberman, Infrared continuum absorption by atmospheric water vapor in the 8-12 μm window, *Appl. Opt., 15*, 2085-2090, 1976.

Rossow, W. B., and L. C. Garder, Cloud detection using satellite measurements of infrared and visible radiances for ISCCP, *J. Clim., 6*, 2370-2393, 1993a.

Rossow, W. B., and L. C. Garder, Validation of ISCCP cloud detections, *J. Clim., 6*, 2370-2393, 1993b.

Rossow, W. B., and A. A. Lacis, Global, seasonal cloud variations from satellite radiance measurements, 2, Cloud properties and radiative effects, *J. Clim., 3*, 1204-1253, 1990.

Rossow, W. B., and R. A. Schiffer, ISCCP cloud data products, *Bull. Am. Meteorol. Soc., 72*, 2-20, 1991.

Rossow, W. B., and Y.-C. Zhang, Calculation of surface and top of atmosphre radiative fluxes from physical quantities based on ISCCP datasets, 2, Validation and first results, *J. Geophys. Res.*, this issue.

Rossow, W. B., C. L. Brest, and L. C. Garder, Global, seasonal surface variations from satellite radiance measurements, *J. Clim., 2*, 214-247, 1989.

Rossow, W. B., L. C. Garder, P. J. Lu, and A. W. Walker, International Satellite Cloud Climatology Project (ISCCP) Documentation of Cloud Data, *WMO/TD-266*, (revised), 76 pp. plus three appendices, World Clim. Res. Programme (ICSU and WMO), Geneva, March, 1991.

Rossow, W. B., A. W. Walker, and L. C. Garder, Comparison of ISCCP and other cloud amounts, *J. Clim., 6*, 2394-2418, 1993.

Salisbury, J. W., and D. M. D'Aria, Emissivity of terrestrial materials in the 8-14 μm atmospheric window, *Remote Sens. Environ., 42*, 83-106, 1992.

Salisbury, J. W., and D. M. D'Aria, Emissivity of terrestrial materials in the 3-5 μm atmospheric window, *Remote Sens. Environ., 47*, 345-361, 1994.

Schluessel, P., W. J. Emery, H. Grassl, and T. Mammen, On the bulk-skin temperature difference and its impact on satellite remote sensing of sea surface temperature, *J. Geophys. Res., 95*, 13,341-13,356, 1990.

Simpson, G. C., The distribution of terrestrial radiation, *Mem. R. Meteorol. Soc., 3*, 53-78, 1929.

Slingo, A., and J. M. Slingo, The response of a general circulation model to cloud longwave radiative forcing, 1, Introduction and initial experiment, *Q. J. R. Meteorol. Soc., 112*, 1027-1062, 1988.

Smith, W. L., H. M. Woolf, C. M. Hayden, D. Q. Wark, and L. M. McMillin, The TIROS-N operational vertical sounder, *Bull. Am. Meteorol. Soc., 60*, 117-118, 1979.

Sohn, B.-J., and E. A. Smith, The significance of cloud-radiative forcing to the general circulation on climate time scale — A satellite interpretation, *J. Atmos. Sci., 49*, 845-860, 1992.

Tarpley, J. D., Estimating incident solar radiation at the surface from geostationary satellite data, *J. Appl. Meteorol., 18*, 1172-1181, 1979.

Toon, O. B., and J. B. Pollack, A global average model of atmospheric acrosols for radiative transfer calculations, *J. Appl. Meteorol., 15*, 225-246, 1976.

Vonder Haar, T. H., and V. E. Suomi, Measurements of the Earth's

radiation budget from satellites during a five-year period, 1, Extended time and space means, *J. Atmos. Sci., 28*, 305-314, 1971.

Webster, P. J., and G. L. Stephens, Cloud-radiation interaction and the climate problem, in *The Global Climate*, edited by J.T. Houghton, pp. 63-78, Cambridge University Press, New York, 1984.

Wick, G. A., W. J. Emery, and P. Schluessel, A comprehensive comparison between satellite-measured skin and multichannel sea surface temperature, *J. Geophys. Res., 97*, 5569-5595, 1992.

Wittmeyer, I. L., and T. H. Vonder Haar, Analysis of the global ISCCP TOVS water vapor climatology, *J. Clim., 7*, 325-333, 1994.

Young, G. S., D. V. Ledvina, and C. W. Fairall, Influence of precipitating convection on the surface energy budget observed during a Tropical Ocean Global Atmosphere pilot cruise in the tropical western Pacific Ocean, *J. Geophys. Res., 97*, 9595-9603, 1992.

A. A. Lacis and W. B. Rossow, NASA Goddard Institute for Space Studies, 2880 Broadway, New York, NY 10025.

Y.-C. Zhang, NASA Goddard Institute for Space Studies, Columbia University, 2880 Broadway, New York, NY 10025.

(Received April 21, 1994; revised October 7, 1994; accepted October 10, 1994.)